AIAA JOURNAL
Vol. 57, No. 8, August 2019

Active Flow Control on Vertical Tail Models

Marlyn Y. Andino* and John C. Lin†
NASA Langley Research Center, Hampton, Virginia 23681
Seele Roman‡
GE Aviation, Cincinnati, Ohio 45215
Emilio C. Graff§
Shaper Tools, Inc., San Francisco, California 94110
Mory Gharib¶
California Institute of Technology, Pasadena, California 91125
Edward A. Whalen**
The Boeing Company, Hazelwood, Ohio 63042
and
Israel J. Wygnanski††
The University of Arizona, Tucson, Arizona 85718

DOI: 10.2514/1.J057876

Active flow control (AFC) subscale experiments were conducted at the Lucas Wind Tunnel of the California Institute of Technology. Tests were performed on a generic vertical tail model at low speeds. Fluidic oscillators were used at the trailing edge of the main element (vertical stabilizer) to redirect the flow over the rudder and delay or prevent flow separation. Side force increases in excess of 50% were achieved with a 2% momentum coefficient (C_μ) input. The results indicated that a collective C_μ of about 1% could increase the side force by 30–50%. This result is achieved by reducing the spanwise flow on the swept back wings that contributes to early flow separation near their tips. These experiments provided the technical backdrop to test the full-scale Boeing 757 vertical tail model equipped with a fluidic oscillator system at the National Full-scale Aerodynamics Complex 40-by 80-foot Wind Tunnel, NASA Ames Research Center. The C_μ is shown to be an important parameter for scaling a fluidic oscillator AFC system from subscale to full-scale wind tunnel tests. The results of these tests provided the required rationale to use a fluidic oscillator AFC configuration for a follow-on flight test on the Boeing 757 ecoDemonstrator.

Nomenclature

A_{act} = normalized exit orifice area
A_{ref} = projected area of wing
AR = aspect ratio
a_o = thin airfoil theory lift slope, $\partial C_{Yn}/\partial\delta_R$ for $2D$
b = span
C_D = drag coefficient
C_L = lift coefficient
C_m = pitching moment coefficient
C_P = pressure coefficient, $(P - P_\infty)/((1/2)\rho_\infty(U_\infty \cos\Lambda)^2)$
C_Q = volumetric flow (incompressible) coefficient, $Q(A_{ref}U_\infty)^{-1}$
C_{Yn} = normalized side force coefficient
C_μ = incompressible momentum coefficient, $2(nA_{act}/A_{ref})(U_{jet}/U_\infty)^2$
C_Π = power coefficient, $Q(P_c - P_\infty)/((1/2)\rho_\infty U_\infty^3 A_{ref})$, with $Q = \dot{m}/\rho_\infty$
c = chord
h_{act} = normalized exit orifice height
$\dot{m}$ = mass flow rate
n = number of active fluidic oscillators
P_c = actuators' plenum chamber static pressure
P_∞ = static pressure of the freestream
Q = volumetric flow rate
Re = Reynolds number based on the mean aerodynamic chord
Sp = spacing between active actuators as a fraction of span, %
U_{jet} = oscillators incompressible speed, $Q/(nA_{act})$
U_∞ = freestream velocity
α = incidence angle, deg
β = sideslip angle, deg
δ_R = rudder deflection angle, deg
γ = specific heat ratio, 1.4
λ = lumped parameter
Λ = sweep back angle at the quarter chord line, deg
μ = pressure distribution changes attributed to active flow control
ρ_∞ = freestream density
τ = skin friction

Received 3 September 2018; revision received 26 April 2019; accepted for publication 9 May 2019; published online 16 July 2019.

*Research Engineer, Flow Physics and Control Branch. Senior Member AIAA.
†Research Engineer, Flow Physics and Control Branch. Associate Fellow AIAA.
‡Research Engineer.
§Product Performance Lead.
¶Hans W. Liepmann Professor of Aeronautics and Bioinspired Engineering.
**Manager, Boeing Research & Technology. Associate Fellow AIAA.
††Professor, Aerospace and Mechanical Engineering Department. Fellow AIAA.

I. Introduction

STEADY blowing for active flow control (AFC) was traditionally used to increase wing lift enabling larger flap deflections without flow separation. Although the use of blowing was driven mostly by the needs of naval aviation, the two popular mass-produced military airplanes relying on it were not intended for ship operation. They were the F-104 and the MiG 21 airplanes. Blowing was used to slow down the landing speed of these airplanes. It did so on the F-104 by taking air from the last stage of the compressor. The system required momentum coefficients, C_μ, of approximately 8% for a reduction in landing speed of approximately 30 mph [1].

The lift increment attained by blowing is supposed to encompass two effects. Momentum is added to the boundary layer to overcome

the frictional losses, thus enabling the flow to proceed along the surface in spite of the adverse pressure gradient. The loss of momentum in the boundary layer is due to viscosity, therefore keeping the flow attached became synonymous to overcoming the detrimental viscous effect. This suggests that added momentum will improve the performance of the wing, increasing it to its inviscid limit and until this is achieved, $\Delta C_L \propto C_\mu$. When the flow is attached and the measured lift approximated the inviscid prediction, the momentum added to the flow by blowing sufficed for separation control. As the momentum coefficient became greater than its critical value for reattachment, $C_\mu > C_{\mu r}$, the lift increment became smaller, $\Delta C_L \propto (C_\mu)^{1/2}$, due to a "jet-flap" effect or a concept that is commonly referred to as "circulation control." The name "jet-flap" appeared because the thin jet departing the trailing edge (TE) of a wing (at a large angle relative to the unperturbed free stream) was initially modeled as a flap extension [2]. The jet curves and approaches the free stream direction with increasing distance from the TE, thus generating a pressure differential across the streamlines marking its borders; hence an increase in jet deflection increases the lift increment. The critical value of $C_{\mu r}$ differentiating separation control from circulation control varies between $2\% < C_{\mu r} < 5\%$. It depends on the specific application such as flap deflection, incidence, thickness of the wing, its shape, sweep and aspect ratio (AR), as well as the extent of the deflected flap and its curvature. When blowing was applied from the shoulder of a highly deflected flap on a symmetrical airfoil whose length was less than 30% of the chord, $C_{\mu r}$ became a function of flap deflection only. Its value was approximately given by: $C_\mu \approx 0.015 \tan(\delta_f)$ (where δ_f is the flap deflection) provided that the angle of incidence is $\alpha = 0°$. Circulation control requires a C_μ that is of the order of 10% although much larger and somewhat smaller values are quoted in the literature [3].

The concept of sequential application of C_μ used for separation control that is followed by circulation control was not seriously questioned to date, although there were indications that should have raised a red flag [1]. Early experiments of blowing through variable slot widths indicated that narrower slots were generating higher lift than wider ones. This suggests that a given C_μ is more effective when it is accompanied by smaller quantity of fluid injected at a greater speed into the stream. Recent experiments [4,5] of blowing and suction from the surface of a blunt elliptical airfoil concurred with that notion providing a new insight into the mechanics of separation control at low values of C_μ. At higher C_μ, blowing generates lift that surpasses the lift generated by suction. It usually occurs when the jet emanating from a two-dimensional slot exceeds the free stream velocity by a factor of three. Around that threshold, a narrow, high-speed jet flowing over the upper surface entrains ambient fluid bending the streamlines toward the surface. In this case, the jet momentum dominates the flow rather than its mass flow rate, enabling one to model its effect by a distributed sink (a line sink in two-dimensional flow). The generation of lift by jet entrainment was demonstrated in 1964 [6]. It indicates that the flow around a flat plate aligned with the stream and a jet emanating tangentially in the midchord of its upper surface curves the streamlines over the upper surface, thus generating circulation and lift. The increase in circulation due to jet entrainment [6] results in a lift increment proportional to $\sqrt{C_\mu}$. This model leads one to conclude that there is no inviscid limit to the lift generated by a wing that uses blowing at incompressible speeds, provided that ample momentum is available for the necessary jet entrainment. Jet entrainment alters the pressure distribution on the surface of a body, thus enabling flow reattachment even under the most adverse conditions [7].

Because jet entrainment is effectively a viscous phenomenon, the classical approach of separating the equations of motion into inviscid and viscous ones no longer applies. In the traditional solution approach, the lift and moment depend on a single lumped parameter, λ. This parameter is defined by the wing contours and its incidence angle, α (i.e., $C_L = C_L(\lambda)$ and $C_m = C_m(\lambda)$). The drag is obtained by using the boundary-layer equations that require an inviscid pressure field to be provided as an input. Thus, $C_D = C_D(\lambda, \tau)$, where τ represents the skin friction integrated around the wing's outer mold line. The introduction of AFC, expressed by a lumped parameter, μ, changes the pressure distribution over the wing as observed above. It also changes the skin friction because a wall-jet or a fluidic oscillator does not interact with a solid surface in the same manner as the free stream does. Hence, $C_L = C_L(\lambda, \mu, \tau)$, $C_m = C_m(\lambda, \mu, \tau)$, and $C_D = C_D(\lambda, \mu, \tau)$. Consequently, the introduction of AFC changes the design space and requires a change in the design procedure. Experiments have shown that:

$$dC_L = \frac{\partial C_L}{\partial \lambda} d\lambda + \frac{\partial C_L}{\partial \mu} d\mu + \frac{\partial C_L}{\partial \tau} d\tau \tag{1}$$

$$dC_m = \frac{\partial C_m}{\partial \lambda} d\lambda + \frac{\partial C_m}{\partial \mu} d\mu + \frac{\partial C_m}{\partial \tau} d\tau \tag{2}$$

Thus, the location of the neutral point on a wing where $dC_m/dC_L = 0$ requires that:

$$\frac{dC_m}{dC_L} = \frac{\partial C_m}{\partial \lambda}\frac{\partial \lambda}{\partial C_L} + \frac{\partial C_m}{\partial \mu}\frac{\partial \mu}{\partial C_L} + \frac{\partial C_m}{\partial \tau}\frac{\partial \tau}{\partial C_L} \tag{3}$$

This equation may entirely change the relationship between a wing and an empennage as it may potentially enable an airplane to remain trimmed over a larger range of lift coefficients by counteracting the effects of incidence with the help of AFC. The deflection of a control surface may be replaced by AFC during some parts of the flight envelope, provided that the reaction time of AFC is sufficiently fast. Thus AFC enables the approach speed of a conventional airplane to be lowered by increasing its lift, alleviates atmospheric turbulence effects, enhances the effectiveness of control surfaces, and perhaps replaces some control surfaces if used differentially on one wing only.

One may now ask whether it is possible to enhance the entrainment capability of a jet. The fluidic oscillator actuation [8–10] provides a plausible answer. Although this paper focuses on the practical question of lift enhancement (or side force enhancement for the vertical tail application), we shall briefly discuss the mechanism of entrainment because it may lead to more effective use of actuators. When two parallel streams of greatly disparate velocities merge, the discontinuity in their velocities at the interface is smoothed by viscosity, creating an inflected velocity profile that is well represented by a hyperbolic tangent [i.e., $(u - U_1)/(U_2 - U_1) = (1 - \tanh y)$, where y is a distance measured across the flow from a location where the velocity is equal to the arithmetic average of the two streams]. The most important characteristic of such a velocity profile is the existence of the inflection point that makes it highly sensitive to an *inviscid instability* described by Kelvin and Helmholtz. This instability is so pervasive that in most aeronautical applications the mixing layer is turbulent, but contrary to other flows, the transition to turbulence retains the shape of the mean velocity profile. The state of the flow notwithstanding, this instability generates an array of large co-rotating eddies that grow in size by engulfing the fluid in their vicinity. The engulfment process is enhanced and made more orderly by periodic excitation introduced at the origin of the flow (i.e., at the separation location). Very small amplitudes are needed to regulate and augment the spatial growth of the instability, and alter the entrainment capability of the mixing layer [11]. The frequency of the excitation determines the streamwise distance required for the eddies to form, their size, their strength, and thus their entrainment capacity. In addition, the reverse flow in long bubbles may create a feedback mechanism that increases the amplification rates in the mixing layer by making it absolutely unstable [12]. Although detailed measurements of the instability are not available, it takes a small amount of reversed flow for that phenomenon to materialize. It is likely to be responsible for flow reattachment.

It was also recognized that boundary layers on the verge of separation and shear layers that have already separated from a solid surface contain similar inflection points in their mean velocity profiles, and they too should be sensitive to the same instability. Increasing the entrainment capability of these flows either lowers the

pressure over the surface by bending the already separated mixing layer to it, or energizes the boundary layer that was about to separate, thus preventing the separation process altogether. Hence, the concept of zero mass flux (ZMF) flow separation control emerged [13,14]. It is also referred to as a "synthetic jet" by others [15].

Experiments were carried out to compare the effectiveness of steady blowing to oscillatory blowing of ZMF, where it transpired that the oscillations substantially reduced the momentum required to attach the flow. In fact, the introduction of ZMF AFC provided the same maximum lift as steady blowing while using only 20% of the momentum input to achieve that task [14]. The ZMF or synthetic jet idea was pursued at numerous laboratories [16–19] and its validity was demonstrated on two airborne vehicles: a "Pioneer" UAV in 1995 and on the XV-15 tilt rotor airplane in 2003 [20,21]. A blower and a rotary valve powered the AFC system in the Pioneer, which oscillate a jet that emerged over a simple flap system. It increased the lift of the vehicle by 17% while requiring a relatively small value of momentum coefficient ($C_\mu < 1\%$). The test on the XV-15 was much more extensive. The ZMF actuation was able to reduce the download created by the rotor wakes on the airplane in hover by enabling the flap to be deflected at an angle that exceeded the natural separation angle by 15°. Coincidentally, the download alleviation was approximately 17% as was the increase in the Pioneer's lift, although the configurations and flight test conditions were different. The "Achilles' heel" of these tests was the actuators that were heavy and needed maintenance. Various actuator types were considered (plasma actuators, piezo-electric, mechanical, shape-memory alloys, etc.) but none were satisfactory. Recently fluidic actuators have been explored more extensively as a practical actuator device.

The use of fluidic oscillators (often referred to as sweeping jets) is practical because they have no moving parts yet the jet emitted sweeps back and forth from one side of the nozzle to the other, therefore interacting periodically with different regions of the boundary layer that is either separated or is about to separate. They seem to be able to entrain ambient fluid effectively although the detail of this process is still unknown. The frequency of the sweeping motion and residence time of the jet at each of the sweep extremities depends on the shape and size of the actuator, as well as the supply air pressure. There are many additional parameters that govern the character of the sweeping motion. The flow inside an actuator and actuator geometry effectiveness were examined at a number of laboratories [8,10,22,23] and have, in some instances, been simulated using computational fluid dynamics (CFD).

A potentially high-payoff application is the vertical tail (or stabilizer) of a twin-engine airplane because its size is determined by the eventuality of losing an engine during takeoff and low-speed climb. The vertical tail represents a large surface that is hardly used under normal flight conditions. It is indispensable during an "engine out" emergency and it is needed during cross-wind takeoff and landing. Although seldom used to its full capability, its presence adds drag and weight to the aircraft, thus increasing fuel consumption. AFC devices that delay flow separation over a highly deflected rudder may enable a smaller vertical tail to provide the control authority needed during an emergency. The broad purpose of AFC is to extend and augment the capabilities of lift generation by flaps and control surfaces beyond the natural separation of the flow. AFC may become a tool that interacts with all the other variables affecting the shape of the vertical tail, but the level of that interaction is still to be determined. A system integration study [24] indicated that such an AFC-enabled smaller vertical tail could result in drag reduction and hence fuel savings.

A series of wind tunnel tests were initiated to establish the efficacy of a system that uses fluidic oscillators at the rudder hinge. It breaks new ground in AFC applications because of the large sweep back of the vertical tail and its relatively moderate aspect ratio. Typical sweep back of the tail surfaces exceed the sweep back of the wing by 10° to 15°. Nevertheless, using AFC for side force enhancement on a vertical tail with a deflected rudder is very similar to lift enhancement on a swept back wing with a deflected simple-hinged flap. Small-scale experiments were carried out on a vertical tail model at low speeds ($U_\infty < 100$ knots) at mean chord Reynolds numbers less than 1.5×10^6. Experiments on a full-scale 757 vertical tail were carried out subsequently at an order of magnitude higher Re. The NASA Environmentally Responsible Aviation (ERA) project was the sponsor of these R&D efforts, where a side force enhancement of 20% was targeted as the success criterion.

The main objectives of these series of tests were to measure the impact of AFC on rudder effectiveness, collect wind tunnel results to enhance the understanding and predictions of AFC application, and highlight challenges for technology transition of an AFC system into a full-scale vertical tail. The scope of these wind tunnel experiments included exploring the variations in AFC actuator's spacing, orientation, pneumatic inputs, as well as variations in wing geometries and flow conditions. This paper highlights key results from these tests, from subscale to full-scale, for advancement of AFC technology to enhance aerodynamic efficiency of a vertical tail.

II. Experimental Setup

A. Facility and Instrumentation

The small-scale experiments were conducted in the Caltech Lucas Wind Tunnel. The 14%-scale model (referred to as AA model) tail was mounted to a force balance inside a boundary-layer plate. The mounting structure sat atop the yaw table. It was shielded from the wind by a fairing mounted rigidly to the nonmetric side of the yaw table. Balance limitations restricted the maximum speed to 40 m/s, corresponding to a Reynolds number of 1.3 million based on the mean aerodynamic chord (MAC). The tunnel features adaptive walls, which in this case were deflected to reduce the blockage introduced by the boundary-layer plate. The local height of the test section above the tip of the tail was 4.5 ft (1.295 m). The width of the test section was constant at 6 ft (1.8 m).

Surface pressure was measured using 230 static pressure taps and an electronically scanning pressure system. These pressure ports were arranged in a spanwise and chordwise grid oriented relative to the leading lead (LE) of the main element and the rudder. The three major chordwise rows feature between 36 and 39 static pressure ports and are located at $z/S = 40$, 70, and 89% relative to their starting point at the LE of the model. A number of additional ports are used to assess the flow in the spanwise direction. The rest of the instrumentation was connected to high-speed acquisition cards using a custom recording software on a personal computer. The air supply was shop air, which provided 100 psig (6.89 bar) capped and 50 SCFM (1415.8 SLPM) at 70 psig (4.82 bar) with a sweeping frequency of 1200 Hz. It was fed to the model by a flexible silicone hose. Forces induced by the hose were evaluated at a variety of capped and flow conditions. They were found to exert a negligible effect. The air supply was controlled by an electronic pressure regulator. Flow was measured by a variable area flow meter. A six-component strain gauge balance was used. The balance has a normal force range of 4000 lb (17.793 N), axial force range of 500 lb (2224 N), and side force range of 1800 lb (8007 N), all within an accuracy of ±1% their respective full scale. Flow visualization was performed using tufts. Force balance data were acquired with and without tufts. The effects of the tufts were evaluated and found to be negligible.

The rudder was built hollow, thus a significant fraction of its volume served as a plenum chamber. This yielded relatively even air supply pressure between the root-most and the tip-most actuators. However, the space was limited on the main element. Static pressure measurements showed that when all of the largest actuators were enabled, a pressure gradient of 10 psi (0.69 bar) existed between the root and the tip. Most of the testing presented here was performed with actuation from the main element. The actuators were machined onto aluminum plates that could be changed. Individual actuators could be disabled by taping shut their inlets from the plenum chamber.

B. Subscale Models

Four vertical tail configurations formed by combining two stabilizers and two rudders were tested (Fig. 1a). The vertical tail AA model has an NACA 0012 airfoil section (see Fig. 1a). The key dimensions of the vertical tail AA model are shown in Table 1. The

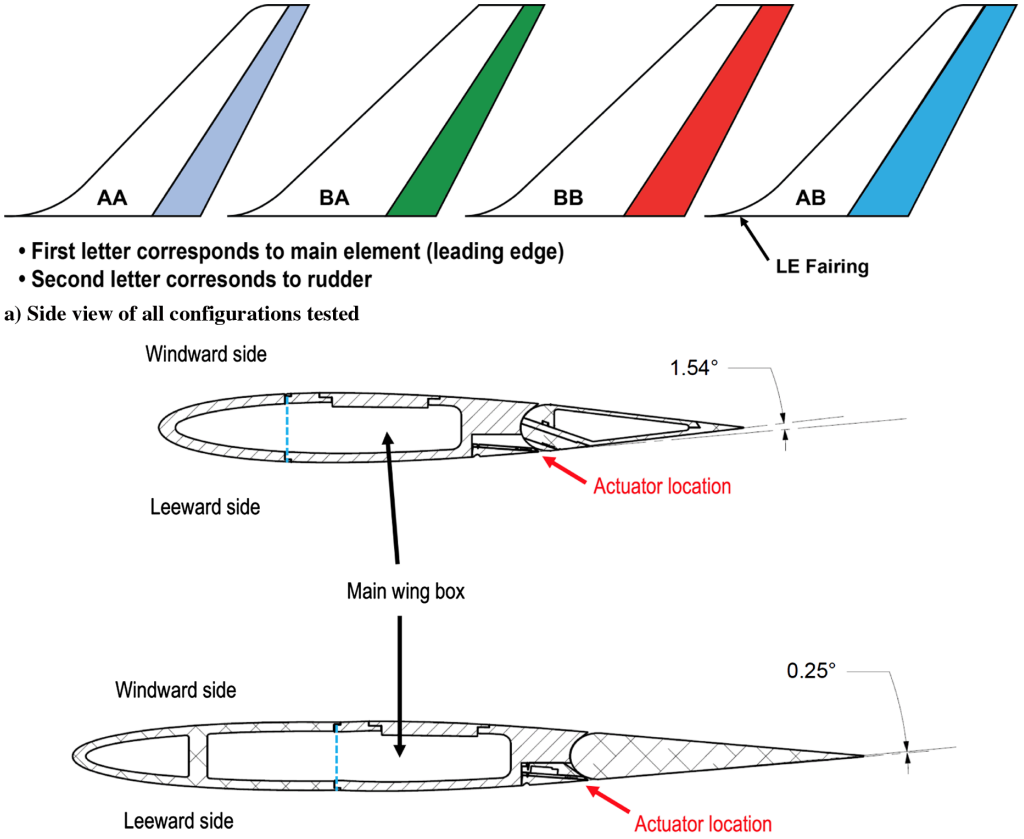

a) Side view of all configurations tested

b) Section view of the AA (top) and BB (bottom) models in the streamwise direction at 30% span

Fig. 1 Four model configurations tested at the Caltech Lucas Wind Tunnel.

leading edge at the root was blended to the horizontal plane with a fairing, as in typical airplane installations. The leading edge (LE) of the vertical tail is swept back ($\Lambda = 43.6°$) with a 35%-chord rudder. The model is 3.5 ft (1.07 m) high with an LE fairing designed to reduce the interaction with the floor boundary layer. Boundary-layer trip dots were installed at 5% chord on the leeward side and at 10% chord on the windward side to eliminate the possible presence of laminar separation bubble on the LE. Rudder angle was achieved by changing brackets external to the outer mold line on the windward side. The angle of incidence changed with the rotation of the yaw table. In all tests, the gap between the main element and the rudder was taped from root to tip to prevent air leakage from the windward side to the leeward side. Notice that this is not a "true" configuration. Commercial airplane tails contain several cutouts on the rudder LE for hinge mounting points. At deflections above 20° to 25°, they are exposed past the seal, allowing a complex airflow to emanate from the openings. This model did not have traditional hinge mounting points, resulting in a smoother rudder leading edge than a typical one on a commercial airplane.

Conversion of the AA model to a BB planform having a 9%-thick airfoil section (NACA009) was achieved by a new leading edge (bottom section view in Fig. 1b) and a new rudder that increase the total mean chord by approximately 34%. There was a slight discontinuity in slope at the juncture to the main wing box (see Fig. 1b). There is also a change in the leeward side of the actual rudder angles because the AA model rudder brackets were reused. The nominal rudder angle is defined as the angle between the plane of symmetry of the main element and the plane of symmetry of the rudder in the original AA model (this is the design angle of the brackets). The angles on the leeward side of each model are in Table 2, with the average difference between the models being approximately 2°.

Table 1 Key dimensions of vertical stabilizer AA model

Description	Dimension
Planform area	0.55 m^2
Planform mean aerodynamic chord	0.54 m
Planform span	1.07 m
Rudder area	0.19 m^2
Rudder hinge position	65% chord
Leading edge sweep back angle (relative to parallel line to span dimension)	43.6°
Rudder hinge angle	33.5°
Trailing edge sweep back angle	27.0°

Because of a fixed rudder hinge angle, the sweep angles are imprecise on the BB model. The root and tip of the leading edge are also approximations to accommodate the existing hardware. Because the trailing edge of the main element remained unchanged, all existing arrays of actuators could thus be reused. These modifications enabled a comparison of the rudder effectiveness of the AA and BB models as well as the AFC effects on them. Two additional hybrid models were constructed by replacing either the leading edge section or the rudder. These changes altered the ratio between the total chord of the vertical tail and the chord of the rudder. The changes in the planform geometry are listed in Table 3. The models are referred to as AA, BB, BA, and AB in future references.

The change of leading edge and rudder increases the scale of the model as the span remained the same. Tests of the AA model were performed primarily at 40 m/s, but tests of the BB model were performed at lower velocity in order to maintain the same Re. The supply air pressure was adjusted when switching the models to assess the influence of the model size and shape on the effectiveness of the AFC at a given C_μ. The significance of the actuator size was shown to be secondary [25]; therefore, the actuator size was not scaled with the particular vertical tail area.

Fluidic oscillators were positioned along the trailing edge (TE) of the vertical stabilizer as shown in Fig. 1b. A maximum of 32 actuators spaced 1.5 in. (38.1 mm) apart (or 3% of the span) and inclined approximately at 170° relative to the upstream leeward-side surface were installed in the model. Although strips of various actuator sizes

and shapes can be easily installed in the model, this paper focuses on the actuators reported in [25] whose nozzle dimensions were 0.040 in. × 0.080 in. (1 mm × 2 mm). All fluidic oscillator actuators were supplied with compressed air through the root of the model. The gap at the juncture between the rudder and the stabilizer was resealed for every rudder deflection.

III. Discussion of Results

A. AA Model

1. Baseline

The study started with the baseline (no flow control) testing of the AA model. Figure 2a shows that as the rudder deflection, δ_R, increases, the slope, $\partial C_{Yn}/\partial\beta$, is reduced. Flow separation over the rudder may occur as the increasing adverse pressure gradient further thickens the boundary layer over the stabilizer. At larger sideslip angles, separation increases ahead of the rudder hinge, showing a decrease in side force versus incidence compared with a constant slope (Fig. 2a). At $\beta = 0°$, the increase of rudder deflection results in an increase of side force; however, $\partial C_{Yn}/\partial\delta_R$ is reduced. This is revealed as the change of side force from each rudder deflection increment is getting smaller and smaller for δ_R of 0° to 40°. The drag polar also indicates that partial separation is present at rudder deflections above 10° at all sideslip angles tested (Fig. 2b). The maximum side force increased with increasing δ_R but so did the drag.

The pressure contours shown in Fig. 3 indicate a highly three-dimensional flow over the rudder. A strong spanwise flow develops over the rudder even at low deflections when the flow is completely attached. Under most conditions the flow is no longer attached near the rudder root. This may be related to the fact that as the rudder deflects, a gap opens between it and the floor, allowing flow from the windward side to seep into the leeward side and generate a junction vortex that redirects the surface flow toward the root of the rudder. It does even more so on a production aircraft due to the fuselage that is generally cylindrical.

2. Momentum Coefficient (C_μ)

The study of the actuation effects involved primarily varying the spacing between active actuators, mass flow rate, and air supply pressure. An actuator spacing of 1.5 in. (38.1 mm, $Sp = 3\%$, 32 actuators) and a fixed rudder deflection of $\delta_R = 30°$ were tested first as shown in Fig. 4a. In the absence of sideslip angle ($\beta = 0°$), an increase in momentum coefficients of up to $C_\mu = 1.9\%$ generates an increase in side force $\Delta C_{Yn} \approx 45\%$ but it also results in a lower stall angle, especially for $C_\mu > 1\%$. The side force generated for sideslip angles $\beta < 10°$ is substantially larger than the values reached for the baseline cases, but at $\beta = 15°$ this advantage disappears. These results show large sensitivity to the sideslip angle, β, that comes from a change in the direction of the flow and an increase in circulation and aft loading caused by the actuation and early leading edge separation. Actuation at $C_\mu = 1\%$ indicates a change in the slope of $\partial C_{Yn}/\partial\beta$ at $\beta = 0°$. This suggests that the flow might be attached at no yaw but the flow over the rudder starts to separate as β increases for the prescribed momentum coefficient, C_μ.

Figure 4b shows that increasing the rudder deflection, for $\beta = 0°$, substantially increases the rudder effectiveness. The stall characteristics of the rudder are shown. In the absence of actuation, the rudder

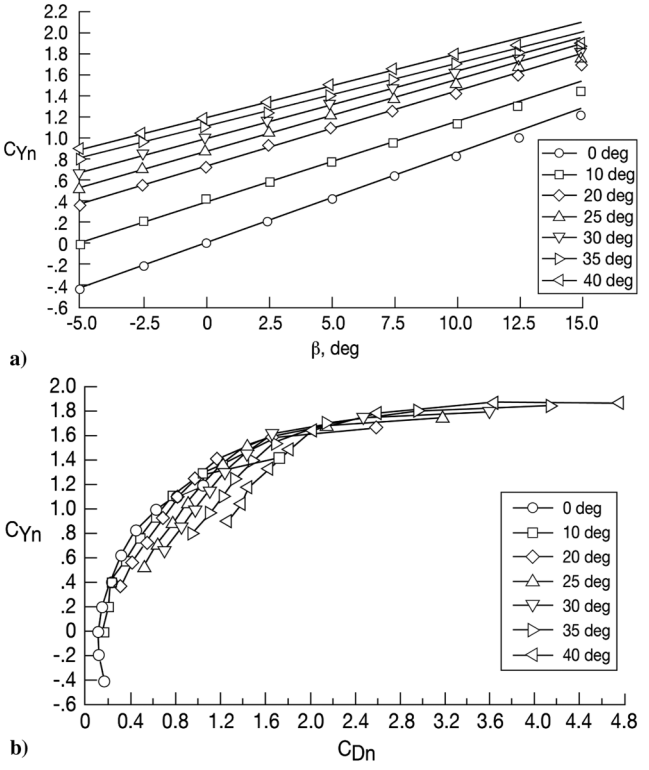

Fig. 2 Dependence of side force on β for rudder deflections varying from $0° < \delta_R < 40°$, flow control off for AA model.

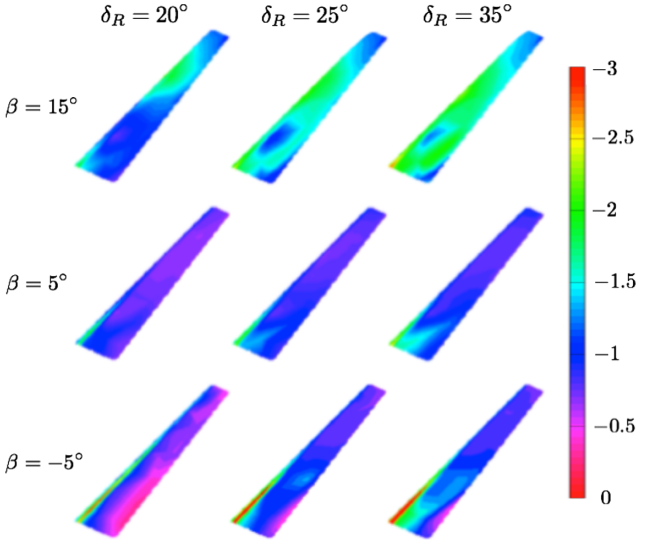

Fig. 3 Pressure coefficient, C_P, contours on the rudder suction side for baseline cases.

Table 2 Nominal rudder deflection in degrees and actual angles of inclination of the suction surface in degrees

Nominal rudder angle, °	AA model, °	BB model, °	Difference
0	1.54	−0.25	1.79
10	10.0	8.2	1.8
20	18.8	16.9	1.9
30	28.0	25.9	2.1
40	37.6	35.5	2.1

Table 3 Geometrical and aerodynamic characteristics of the four models tested

Model	Mean chord, mm	Rudder chord, mm	Wing area, S, m^2	X_H/c	Λ_{LE}, °	Λ_{TE}, °	Θ_H, rad	Σ	AR	$(\partial C_L/\partial\delta)(100) - 1$, $C_\mu = 1.5\%$
AA	541	189	0.546	0.65	43.6	37	1.875	2.220	4.18	2.0
BB	727	254	0.725	0.65	46.5	34.5	1.875	2.220	3.14	1.92
BA	663	189	0.660	0.72	46.5	37	2.026	2.013	3.44	1.76
AB	606	254	0.611	0.58	43.6	34.5	1.734	2.397	3.74	2.16

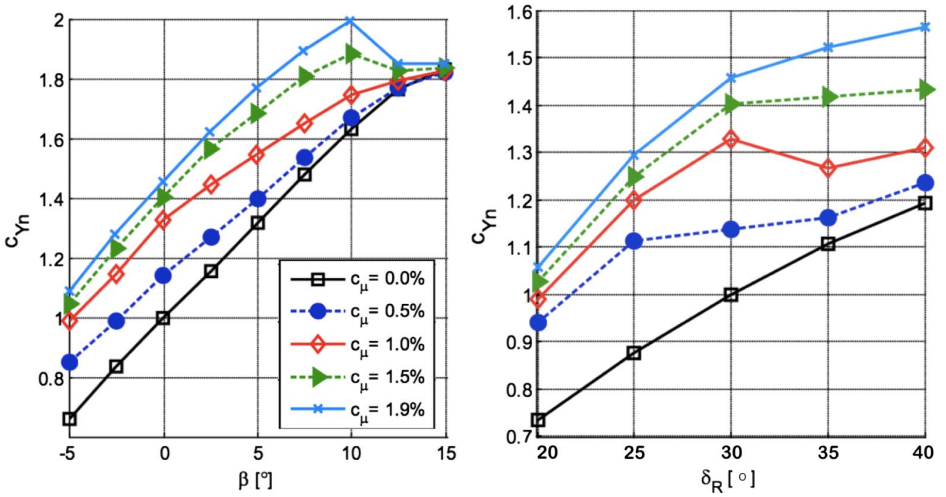

a) C_{Yn} vs β for a rudder deflection, $\delta_R = 30°$ b) C_{Yn} vs δ_R for a sideslip angle, $\beta = 0°$

Fig. 4 Change in side force at $U_\infty = 40$ m/s with actuator spacing of 1.5 in.

is partially stalled for the range of rudder deflections shown (i.e., $\delta_R > 20°$) but the separation is three-dimensional. Therefore, the slope of $\partial C_{Yn}/\partial\delta_R$ is low but it is approximately constant. At $C_\mu = 0.5\%$ the flow is attached to the rudder at $\delta_R = 25°$ and then it stalls more uniformly along the span, resulting in $\partial C_{Yn}/\partial\delta_R \to 0$. At $\delta_R = 35°$ the flow over the rudder is fully separated for this actuation level and the added benefit becomes insignificant. Increasing the actuation level to $C_\mu = 1\%$ results in the rudder stalling at $\delta_R = 30°$. The partial separation from the rudder can be ameliorated by increasing the momentum coefficient even further but some separation over the rudder persists at larger deflections unless C_μ is increased beyond 2%.

The chordwise pressure distributions over three sections for the rudder deflected at $\delta_R = 30°$, with a spacing of 1.5 in. (38.1 mm, $Sp = 3\%$, 32 actuators) is shown on Fig. 5. The baseline flow is separated over the rudder at all three sections. The inboard section shows flow separation over the rudder for all actuated cases. As described previously, there is a gap between the rudder and the tunnel floor at this rudder deflection. This allows for air to pass from the windward side to the leeward side. It results in a strong streamwise vortex that could not be eliminated by AFC. In the absence of actuation, it creates a pressure distribution similar to a one associated with a bubble in 2D flow. The increase of momentum coefficient in this area does not reduce flow separation but it reduces the presence of the juncture vortex seen in the absence of actuation. This vortex reduction led to less obstruction of the streamwise flow that resulted in higher suction pressure on the leeward side and the associated increase in side force. An increase of C_μ from 0.5 to 1.9% accomplishes little at the TE of the rudder inboard section but it increases the suction peak near the rudder hinge. The middle and outboard sections show attached flow or reduced separation for $C_\mu > 1\%$.

3. *Actuator Spacing and Power Coefficient (C_Π)*

The differences in overall performance as a function of actuator spacing can be significant as shown in the ΔC_{Yn} versus power coefficient (C_Π) curves $\delta_R = 20°$ and 30° in Fig. 6. As the rudder deflection increases, high spacing between jets maintains a steep slope in the C_{Yn} versus C_Π input curves, but tighter spacing can offer higher maximum benefits at large C_Π. At a rudder deflection of 20° (Fig. 6a), which shows little or no separation, a side force increase is still possible at all spacings. At $C_\Pi < 0.01$, the largest spacings provide the largest side force but there is a crossover around that threshold where the smallest spacing provides the largest ΔC_{Yn}. At 30° rudder deflection (Fig. 6b), larger spacing is favored at $C_\Pi < 0.04$. As the rudder deflection increases, the advantage of large spacing becomes more distinct. The steep slopes are maintained at large spacings when in some cases they generated significantly more side force than small spacing cases at the same C_Π levels. The increase in side force caused by the smallest actuators at $\delta_R = 20°$ and $\beta = 0°$ was 13.5% when the spacing was 15% (6 actuators) and a mere 2.8 psig (0.19 bar) pressure was applied to the plenum chamber.

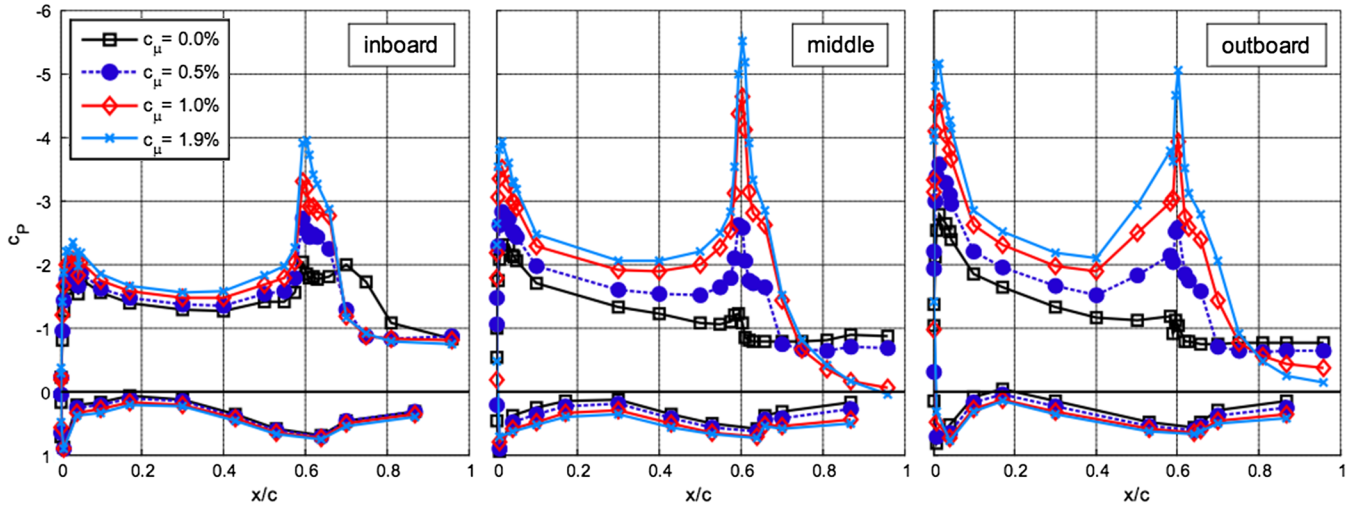

Fig. 5 Chordwise pressure distributions at $U_\infty = 40$ m/s with actuator spacing of 1.5 in. (38.1 mm) for sideslip angle, $\beta = 0°$, and rudder deflection, $\delta_R = 30°$.

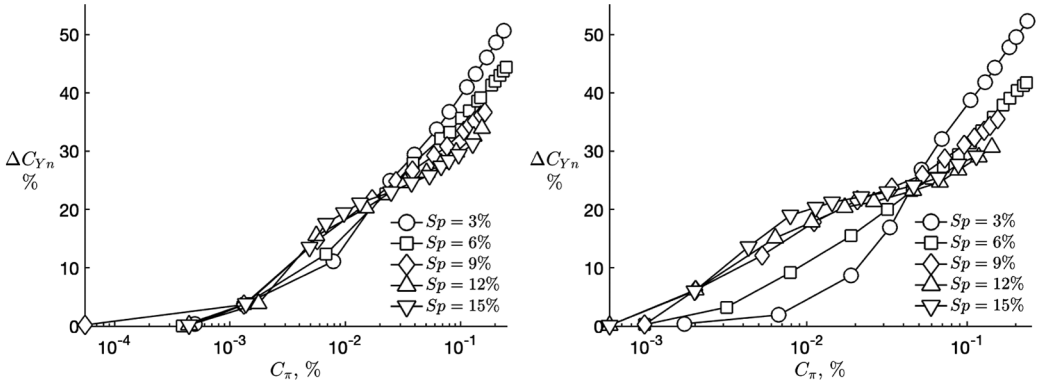

a) $\delta_R = 20°$ rudder deflection b) $\delta_R = 30°$ rudder deflection

Fig. 6 Change in side force as a function of power and actuator spacing for the AA model.

A ΔC_{Yn} of 18% is achieved at just over twice this pressure. At spacings $\geq$ 9% (9 actuators), there is a large increase in side force at low input where there is less effect on reattaching the flow over the rudder. This would probably result in minimal benefit in drag.

Tests were also conducted with vortex generators installed on the main element. Rectangular vortex generators were installed along the 45%-chord line at a spacing corresponding to $Sp = 6\%$ (16 vortex generators) of the span. They were angled perpendicular to the local surface and the rudder hinge. They were 5 mm tall and 15 mm long. When the side force generated by a rudder does not meet expectations on a shorter (fuselage) variant of a commercial aircraft family that shares the same tail design as the longer variant, it is sometimes remedied by placing vortex generators on the vertical stabilizer to provide additional side force needed to compensate for the shorter moment arm between the tail and the center of the gravity of the aircraft. This was done recently on a commercial transport aircraft; consequently it was interesting to check how AFC performance compares with that of the vortex generators where the latter could be made deployable for future control. In Fig. 7, the pressure contours show that when vortex generators are placed along the entire span ahead of the rudder, the flow over the rudder becomes more uniform. At rudder deflection of 20°, the vortex generators manage to get the flow attached as shown in the pressure recovery at the trailing edge of the rudder. The suction pressure is increased by the vortex generators near the hinge (leading edge) of the rudder for both angles shown and that resulted in an increase in side force but unfortunately was accompanied by an increase in drag. Of note is that AFC with a spacing of 6%, corresponding to the placement of the vortex generators in Fig. 7, can generate an increase in side force of 13.2% without increasing drag. At the same rudder deflection, vortex generators increased side force by 11% but with a 9% increase in drag. The low drag increase was due to the AFC device-induced

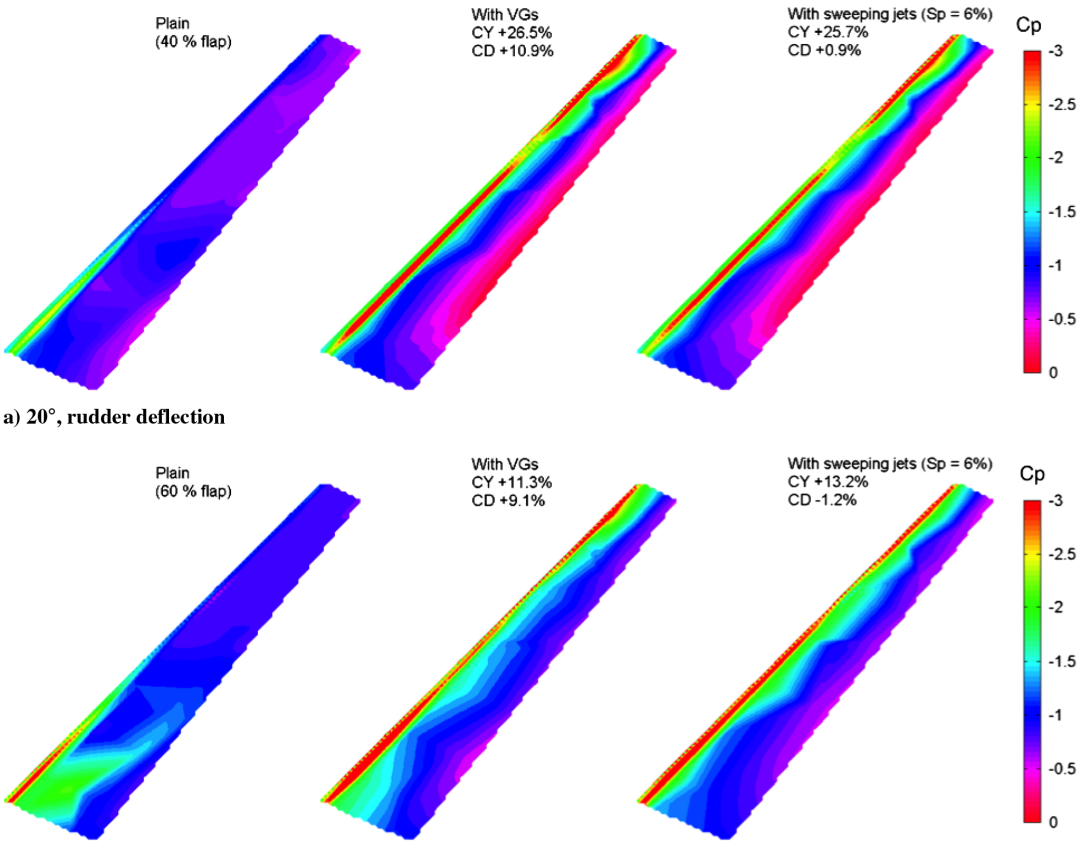

a) 20°, rudder deflection

b) 30°, rudder deflection

Fig. 7 Comparison of pressure contours on the rudder for baseline (left), vortex generators (middle), and fluidic oscillators (right) for two rudder deflections.

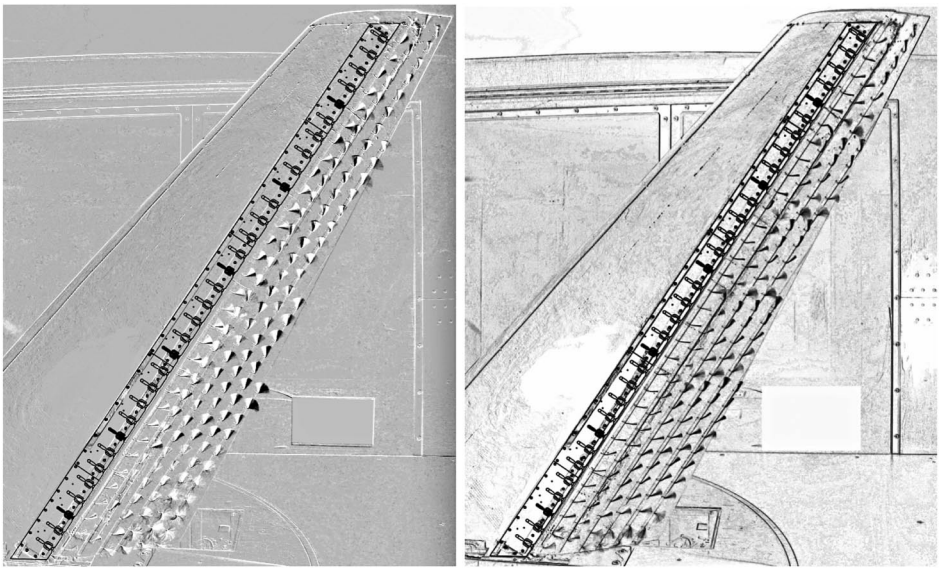

a) $C_\Pi = 0.002$ b) $C_\Pi = 0.167$

Fig. 8 Difference image for $\delta_R = 20^\circ$ rudder deflection, $\beta = 0^\circ$, $A_{\text{act}} = 1.0$, $Sp = 15\%$. The flow is from left to right.

thrust counteracting a relatively small value of drag (axial) force. For the same increase in drag, the fluidic oscillators can generate nearly four times the side force increase.

One simplified model to explain the behavior of a case where the actuators are densely spaced is that the fluidic oscillator, with its oscillatory behavior, is "saving power by extending actuation into the time dimension." Because the sweeping frequency is so much higher than any characteristic frequency in the flow, as far as the flow is concerned, the fluidic oscillator is blowing in all directions at once. This leaves very little rudder area directly unaffected by actuation similar to the coverage produced by a continuous slot, and even those regions that are not directly blown are seeing a significant change in the flow field due to the entrainment of the surrounding jets. But from the point of view of the power source, only a fraction of the actuation is being blown at any given time, and so power (mass flow) savings resulted.

When actuation is sparse (Fig. 6), most of the side force increase comes at very low C_Π ($\partial C_{Yn}/\partial C_\Pi \gg 1$). This is an interesting regime because of the implications that a significant side force increase can be achieved at minimal power input—certainly significantly lower than that of blowing through a slot. At low C_Π, the actuator sweep angle is maximized, and tuft images show that the side force increase comes from the redirection of otherwise significantly spanwise flow over the rudder toward the direction of the free stream (Fig. 8a). The difference is slight but it covers almost the entire rudder outside the base vortex that is caused by the gap between the deflected rudder and the floor. Figure 8a shows the difference between tufts for the baseline case and for the case of actuation with $C_\Pi = 0.002$ ($P_c = 2.8$ psig, 0.19 bar), resulting in a 16.7% increase in side force over baseline. The white and black regions indicate the position of the tufts with and without actuation, respectively. Contrast is a measure of the physical displacement in the tufts; that is, gray indicates a small difference (where tuft locations overlap). The locations of the active fluidic oscillator jets are shown in solid white; the rest are outlined. The root-most jet has little effect on the flow near the root. Similar conditions with near maximum power coefficient, $C_\Pi = 0.167$, are shown in Fig. 8b. The figure shows the tufts with the actuators on and a background image subtracted to highlight the formation of spanwise cells of flow created by the high-speed jets. At these higher jet speeds, the root-most jet is able to contribute significantly to stabilize the flow near the root of the rudder. At higher C_Π, the individual jets become very distinct and the flow over the rudder is divided into pockets (cells). The three-dimensionality of the flow becomes very evident as the topology of the flow changes somewhat along the span as a result of taper and finite AR. In the outer half of the tail, most cells are actually seen to have reverse flow near the inboard edges of the jets.

The crossover point at which the benefits of the sparsely spaced actuators decrease and the benefits of densely spaced actuators increase depends on the number of actuators used at low C_Π and on rudder deflection (Fig. 6). In the case of these tests, where the spacing could only be changed in a discrete manner with a minimum change of 3% of the span, the beginning of the sparse regime is already evident at a spacing of 6% at $\delta_R = 30^\circ$ and it seems to be completed at a spacing of 9%. The trends remain through the maximum spacing tested (15%). The trends observed in the sparse case can continue into extreme cases of three (or even less) jets populating the entire span. One would suspect a different behavior; that is, if a single jet is able to increase the side force by 5%, then it must be due to the interruption of the spanwise flow field over the rudder. This is an important implication for highly swept wings where a performance increase can be had even in cases where little or no separation exists simply by preventing long stretches of spanwise flow and, if possible, redirecting the flow globally in a streamwise direction. Such was known by designers that employed fences on wings of airplanes like the Trident [26] to prevent tip separation at the higher angles of attack seen during takeoff and landing. Being able to achieve the effect with a jet that can be turned off or moved to another location at will has obvious advantages.

The actuator orifice area can be changed by scaling the entire geometry. This has packaging implications. For many conditions, the differences in performance for different sizes of actuators are small. This means that, in certain circumstances, a choice of actuator sizes gives the designer the option to tune the system to the available air supply and packaging constraints. Traditional airplane design provides for bypass air as the source of power for many high-powered systems. A high-flow, low-pressure setup will usually necessitate a larger number of actuators. However, modern aircraft have followed trends seen also in shipbuilding, where the primary form of distribution of power is electric even for high-power systems. In such applications, a compressor can be chosen to generate the characteristics that best benefit the system. This will usually tend toward high pressure and low flow because the actuators will be smaller and pressure losses over long runs will be reduced. In a tightly constrained system, a combination of size and spacing must be used to tune the actuation system to the power source available.

4. *Actuator Orientation*

An evaluation was carried out to demonstrate that the sweeping effects of the fluidic oscillators are secondary for large spacing and

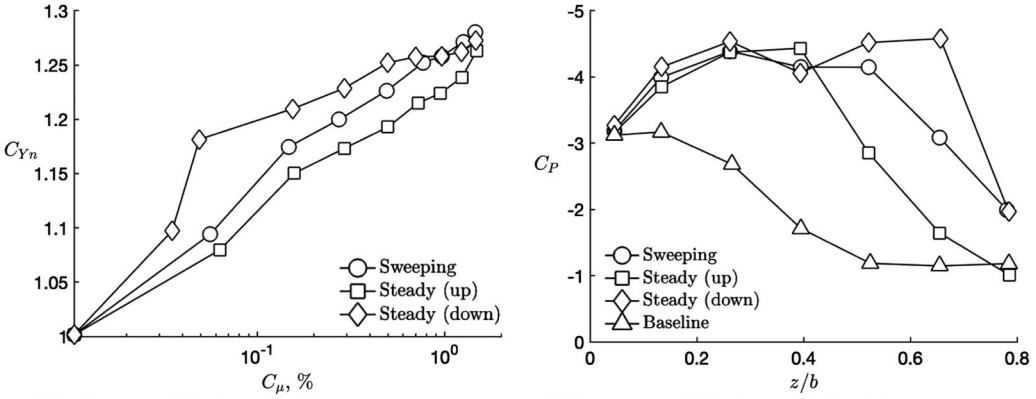

a) Side force coefficient **b) Pressure coefficient near rudder hinge**

Fig. 9 Effect of steady jets and jet orientation on model AA ($Sp = 12\%$, $C_\mu = 0.3\%$, and $\delta_R = 30°$).

low momentum coefficient at zero sideslip conditions. This evaluation was performed by blocking one of the two feedback channels of the actuators to produce nonoscillating steady jets inclined to only one side of the exit nozzle. Two new actuator configurations were obtain: one with all steady jet exits inclined toward the tip of the wing (up), and another with all steady jet exits inclined toward the root of the wing (down). The dependence of C_{Yn} corresponding to each of the conditions tested on C_μ is shown in Fig. 9 for $Sp = 12\%$ and $\delta_R = 30°$. It is clear that steady jets inclined toward the root of the rudder generate the largest side force for a prescribed low C_μ input. The difference in the direction of the steady jets provided a 5% difference in C_{Yn} at $C_\mu \approx 0.25\%$, while the fluidic oscillator actuation halves the difference. Because the fluidic oscillators' results are bracketed by the two steady jet results that differ in their orientation, the effect of the sweeping motion was deemed to be secondary in this case, whereas the jet direction relative to the hinge angle might have been more significant.

B. Other Subscale Models

1. Baseline

After the initial testing of the AA model, three additional model planforms were also tested. These model planforms (i.e., BA, BB, and AB) are illustrated in Fig. 1a. In this study, the models differed in rudder hinge locations and in their aspect ratio while retaining many of the parameters associated with AFC. The purpose of changing the planform of the tail model was to prove that large benefits of AFC can be derived by involving it in the preliminary design and sizing procedure. This is a departure from the prevailing philosophy that uses AFC as a device of last resort to augment the performance of a wing at low speeds.

The dependence of the side force on rudder deflection (δ_R) is plotted in Fig. 10a for all four models. The C_{Yn} was normalized by the appropriate planform area of each vertical tail and the results of models AA and BB were compared at identical Reynolds numbers. The first task was to attempt an explanation for the difference in rudder effectiveness between these two models whose rudder hinge is at the same location relative to the chord ($x_H/c = 0.65$). The model BB has a lower AR and its rudder is deflected at slightly lower δ_R (see Table 2 and Fig. 1b) because the same brackets were used to hold the respective rudders. Both factors could have provided a slightly lower C_{Yn} relative to model AA unless separation is involved, and hence the larger rudder chord and slightly smaller δ_R of the BB model (Table 3) work in its favor.

The side force generated by model AB whose hinge is located at $x_H/c = 0.58$ is approximately 12% larger than the C_{Yn} generated by model BB ($x_H/c = 0.65$) at $\delta_R = 30°$ although both use the same rudder and the same hinge brackets. The difference in this case can be explained using potential flow. The thin airfoil theory will attribute part of the difference in rudder effectiveness to different locations of the hinges, yielding $\Sigma_{AB}/\Sigma_{BB} = 1.08$ (see Table 3), whereas some additional differences stem from the different aspect ratios and real flow effects. One such effect is the interaction between the vertical tail and the tunnel floor. In this case, the floor boundary layer generates a "necklace vortex" around the vertical tail. This vortex is further reinforced by the gap between the rudder side edge at its root and the floor. This gap allows air to seep from the high-pressure side of the rudder's root to the low-pressure side. The magnitude of these effects is not small and it results in a nonlinear $\partial C_{Yn}/\partial\delta_R$ seen in Fig. 10a. The primary difference in the effectiveness of model AA and model BA is attributed to the hinge location that is moved further to the rear (from $x_H = 0.65$ to 0.72) when switching from AA to BA. Thus, simple potential two-dimensional calculations can provide a guide for the effectiveness of a finite swept back wing although they cannot provide a definitive answer due to the complexity of the overall geometry.

The drag polars shown in Fig. 10b indicate that the short chord rudder used in configurations AA and BA is least effective. It provides the lowest side force while generating the highest drag. The

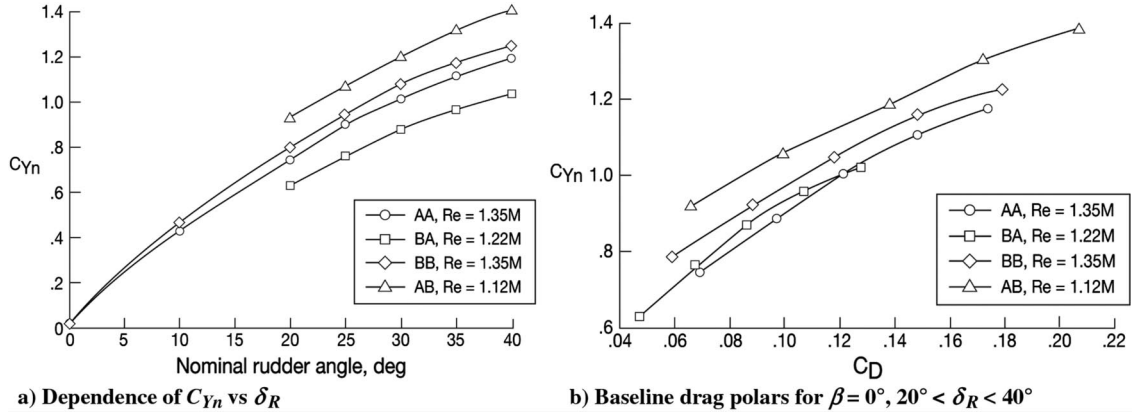

a) Dependence of C_{Yn} vs δ_R **b) Baseline drag polars for $\beta = 0°$, $20° < \delta_R < 40°$**

Fig. 10 Dependence of side force and drag polars on nominal rudder angle for all four vertical tail configurations.

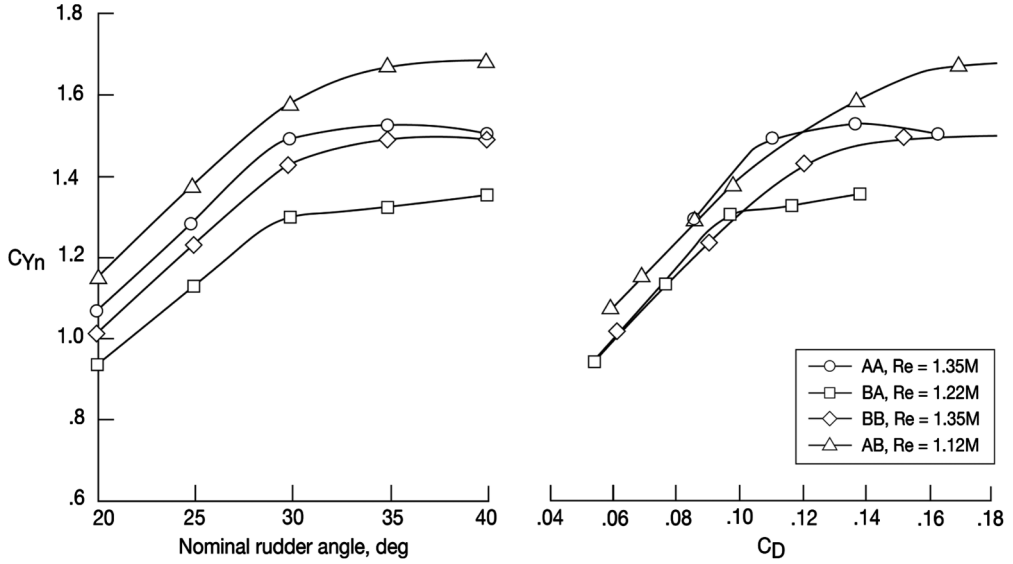

Fig. 11 Effect of AFC ($C_\mu = 1.5\%$) on C_{Yn} and C_D produced by the four vertical tail configurations.

BB model performs better, but the AB hybrid model performs better than the rest. C_{Yn}/C_D for the AB model is 30% better than the AA model at $C_{Yn} = 1$. The difference is primarily attributed to flow separation on the shorter chord rudder whose upper surface is inclined at $\Delta\delta_R \approx 2°$ more than the longer chord rudder. Consequently, in the absence of AFC, the most effective vertical tail among the four models chosen is configuration AB whose hinge is located at $x_H/c = 0.58$ with an aspect ratio of 3.74.

2. *Momentum Coefficient (C_μ)*

One may take full advantage of AFC, as a tool in preliminary design, knowing at the start that compressed air of a prescribed pressure and mass flow rate are available. Let us assume that during the sizing and selection of a vertical tail we can incorporate AFC into the design at momentum coefficient values of the order of 1% ($C_\mu \approx 1\%$). This is to find out if the introduction of fluidic oscillators alters the choice of a vertical tail. If the low level of C_μ attaches the flow, it should make inviscid estimates more reliable while avoiding complexities associated with supercirculation that requires momentum coefficients that are an order of magnitude higher, that is, $C_\mu \approx 10\%$.

The results shown in Fig. 11 suggest a linear dependence of C_{Yn} on δ_R for $0 < \delta_R < 30°$. In fact, the slope is almost constant up to $\delta_R = 30°$ for all the models, indicating that the flow should be attached over the rudder at those deflection angles with $C_\mu = 1.5\%$. One may observe that model AA provides a higher side force and thus a higher $\partial C_{Yn}/\partial\delta_R$ than model BB (see Table 3 last column). Because the rudder hinge is located at the same fraction of the chord and both airfoil sections are thin, the two-dimensional $(\partial C_{Yn}/\partial\delta_R)_{2D} \equiv a_o$ should be identical for both models AA and BB. The most likely difference in the slope of the curves is due to the difference in aspect ratio (AR) of the vertical tail models. Using the well-known relationship derived by Prandtl in 1915 [27] ($\partial C_{Yn}/\partial\delta_R = a_o/[1+(a_o/(\pi\mathrm{AR}))]$), one obtains that $a_o = 2.37 \pm 0.01$ for both AA and BB models.

Comparing the results shown in Fig. 11 to the baseline results (Fig. 10), one realizes that model AB is most effective with or without AFC. However, the level of the effectiveness depends on AFC. For example, at $\delta_R = 30°$ model AA generated $C_{Yn} \approx 1.5$ when $C_\mu = 1.5\%$ corresponding to $C_D = 0.108$. Configuration AB generates identical drag at the same C_μ but at a lower rudder deflection (Fig. 11). If the affordable C_D is the limiting factor, then the baseline configuration AB generated a C_{Yn} that is approximately 20% larger than configuration AA (Fig. 10). Consequently, an optimization procedure is required as comparison of percentage improvement due to AFC at a predetermined input C_μ is inadequate, because it would lead to a faulty preference of configuration AA (see Fig. 12). The addition of fluidic actuators made the rudder stall more distinctive at $30° < \delta_R < 35°$ due to the AFC interfering with the spanwise velocity component. Notice that the side force increases as the area is reduced. Thus, if the maximum rudder deflection is limited to $\delta_R = 25°$, densely spaced actuators using a total $C_\mu = 1.5\%$ would enable a side force increase of 37% and resulting in a potential tail's surface area reduction of 27% (i.e., $100\% \times (1 - (1.37)^{-1})$). If, however, one would have a limited choice between model AA and model BB, one would choose the latter in the absence of AFC and the former in its presence, therefore increasing ΔC_{Yn} by 0.40. The substantial increase in ΔC_{Yn} does not increase the total drag significantly in spite of the large increase in the drag component resulting from the increase in side force. Thus, the introduction of AFC into the preliminary design process may affect the choice of the wing planform selected for the application and its ultimate performance.

The introduction of fluidic oscillators in the design process brings a variety of new flow parameters whose precise effect on the side force generated is still unknown. They relate to the location of the actuators, their total number, their size, their nozzle aspect ratio, and the spacing between adjacent actuators. All of these interact with the model shape, its incidence, and its rudder deflection. In the following section we shall examine further some of these parameters and their effect on the control authority of the rudder.

The increases in C_{Yn} generated by increasing C_μ for closely spaced actuators located at the trailing edge of the four vertical stabilizers planforms are shown in Fig. 12. The AA and BB models respond in a similar fashion to the increase in C_μ for the three rudder deflections. Although at low C_μ and $\delta_R \geq 30°$ model AA produces slightly lower C_{Yn}, it produces higher side force than model BB at higher C_μ. The crossover point between the two requires higher C_μ at higher rudder deflections (see Fig. 12b). This is because closely spaced actuators add momentum to the chordwise flow, thus delaying separation. More momentum is required at higher rudder deflection angles as the adverse pressure gradient in the chordwise direction is larger. The highest absolute value of C_{Yn} is generated by model AB, implying that the relative chord of the rudder should be increased regardless of any other consideration but the relative increase in $\%\Delta C_{Yn}$ is deceiving. For example, while model BA provides the largest $\%\Delta C_{Yn}$ at $\delta_R = 35°$ and $C_\mu = 3\%$, it also provides the worst baseline results. The low baseline coupled with large increases of ΔC_{Yn} due to AFC at all values of C_μ and δ_R investigated skews $\%\Delta C_{Yn}$ in its favor. It diminishes the perceived value of AFC because it implies that is does best when the baseline design is worst. One may also observe in Fig. 12 that at $\delta_R = 20°$ the smallest values of C_μ increase C_{Yn} but at $\delta_R = 30°$ a minimum threshold value of C_μ is required before any noticeable increase in C_{Yn} would be observed. If we divide $\Delta C_{Yn}/C_{Yn\,\mathrm{Baseline}}$, model AB would be by far the worst

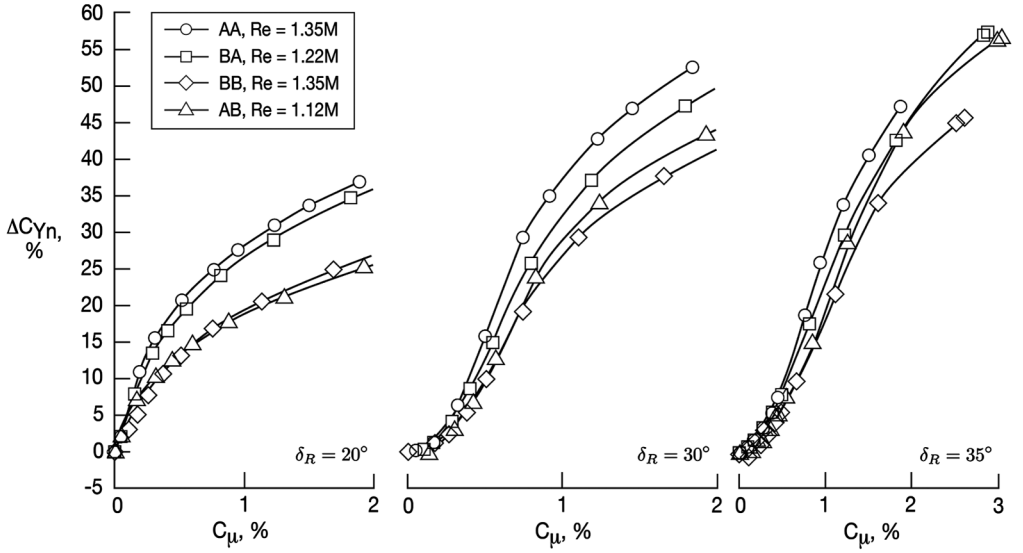

a) ΔC_{Yn} for $\beta = 0°$

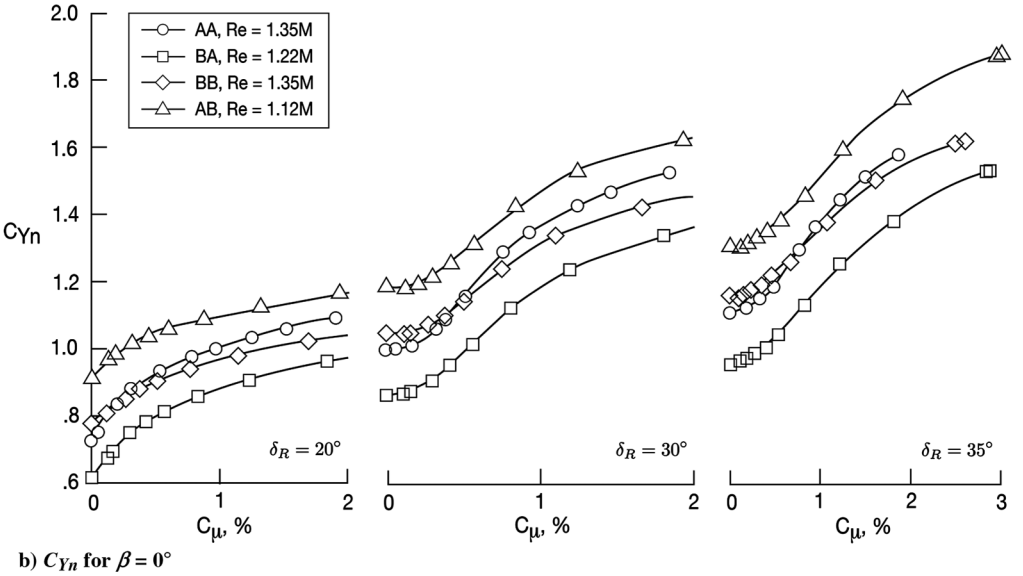

b) C_{Yn} for $\beta = 0°$

Fig. 12 Variation of C_{Yn} and ΔC_{Yn} with C_μ at $\delta_R = 20°, 30°$, and $35°$ rudder deflections, $A_{act} = 1$ and $Sp = 3\%$.

performer as far as AFC is concerned, not because ΔC_{Yn} is the worst but because its baseline C_{Yn} is the best. This effect is stressed because the value of AFC is generally evaluated by improved performance for a prescribed design.

The results shown in Fig. 13 compare the percentage improvement attained for the four configurations at $\beta = 7.5°$ and $\delta_R = 20°, 30°$, and 35°. This figure shows the mandatory success criteria of 20% side force enhancement as defined at the initiation of the project. To achieve a prescribed $\%\Delta C_{Yn}$ improvement at $\beta = 7.5°$ is more demanding than at $\beta = 0°$, not because the contribution of AFC is substantially different but because the baseline results are different. Clearly model AB would have supplied a much higher C_{Yn} (Fig. 12b), but according to the "success criteria," it is the poorest performer (Fig. 13). A much more realistic approach would be to specify for a given sized wing and a prescribed C_Y required for the entire flight envelope and assign the configuration that meets all those needs when at minimum C_μ.

Cruise drag in normal cruise is of great significance in airplane design because the largest percentage of aircraft operation time is spent in cruise, but the significance of drag on a deflected vertical tail is of utmost importance if one engine stops during cruise over the ocean (ETOPS). Drag was measured and the results are shown in Fig. 14. Drag is initially reduced at all values of C_μ for all angles of rudder deflection considered. An increase in C_μ reduces the drag until the flow becomes fully attached. The side force generated by enhanced entrainment of fluid over the rudder's suction surface also increases the induced drag affecting the entire drag force. The C_μ required to attach the flow and minimize the drag increases varies with increasing rudder deflection, δ_R. It is only 0.2% at $\delta_R = 20°$, and it varies between 0.5 and 0.9% at $\delta_R = 35°$ depending on the model geometry. The highest reduction in C_D was generated by model AB at $\delta_R = 30°$. It was also the rudder deflection angle where all other models attained their maximum drag reduction (i.e., where ΔC_D was minimum). Fluidic oscillators managed to reduce the drag by 0.012 on the AB model but only by 0.004 on the BA model. The former has a small stabilizer and a large rudder. Most of the drag is attributed to flow separation and the associated "form drag" due to smaller base pressure. The BA model represents the opposite extreme to the AB model with skin friction on the larger stabilizer being a larger contributor to its total drag. The drag polars shown in Fig. 14b had the C_μ used added to the drag measured (see the abscissae of Fig. 14b), presuming that it could be otherwise used to generate thrust. The baseline drag of model BA is the lowest in all cases considered. This suggests that skin friction contributes much less to the overall drag than low base pressure. Therefore, the introduction of AFC to model BA may be useful at moderate side force coefficients; however, the effectiveness of the total system has to be optimized first.

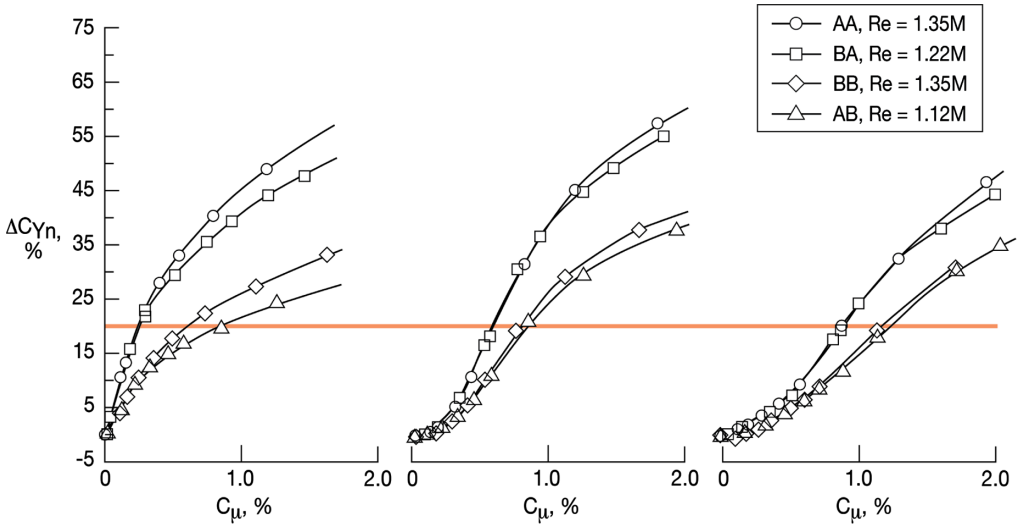

Fig. 13 Percentage improvement in C_{Yn} by increasing C_μ at $\delta_R = 20°, 30°$, and 35° rudder deflections, $\beta = 7.5°$, $A_{act} = 1$ and $Sp = 3\%$.

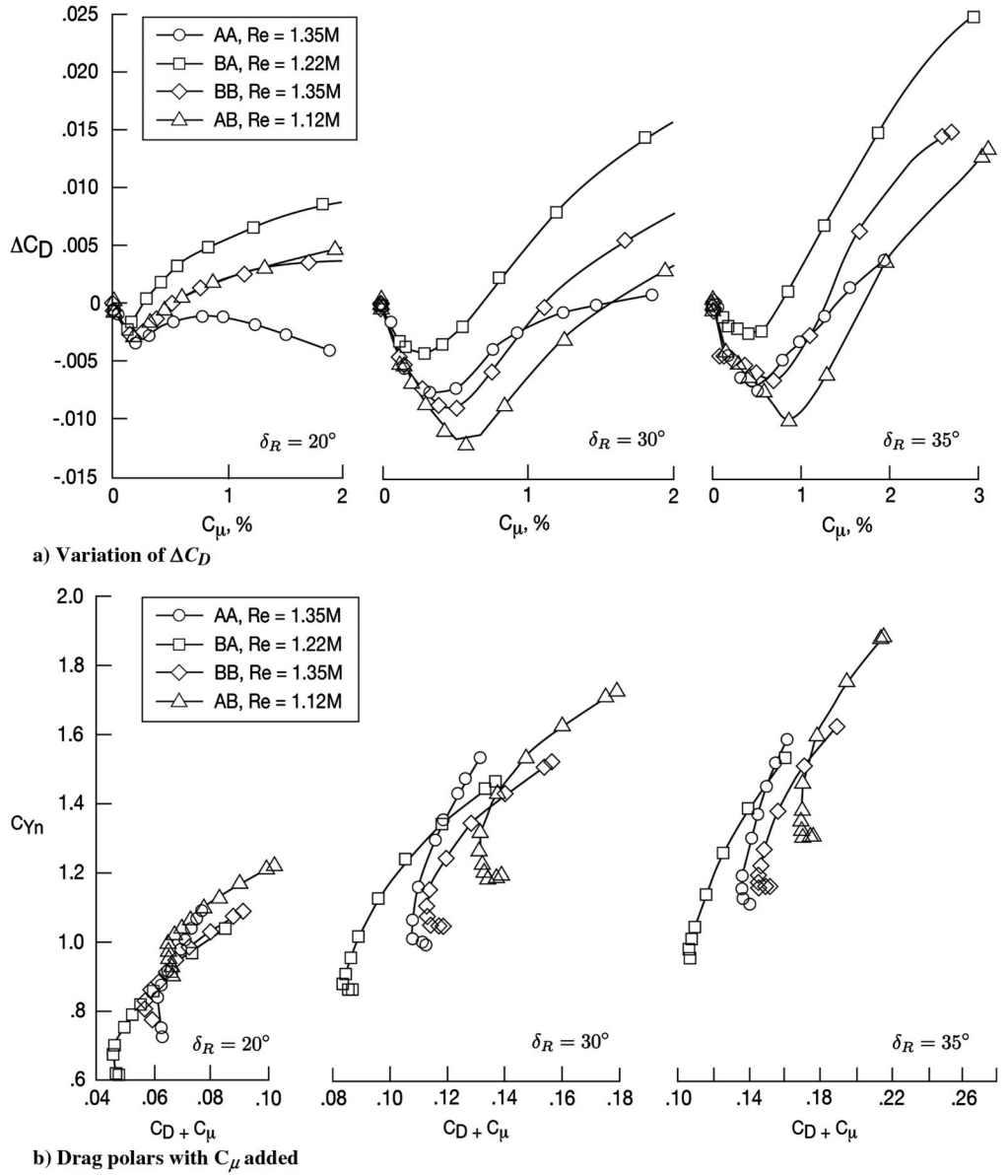

Fig. 14 Drag characteristics for the four planforms at $\delta_R = 20°, 30°$, and 35° rudder deflections, $\beta = 0°$, $A_{act} = 1$, and $Sp = 3\%$.

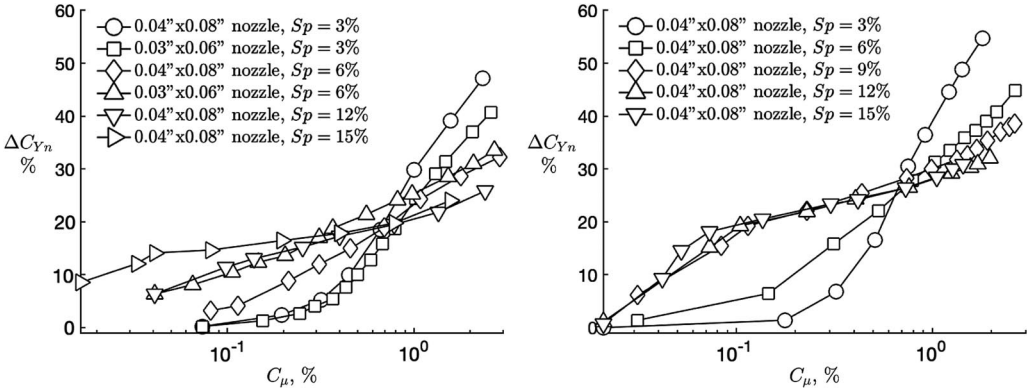

a) Configuration BB **b) Configuration AA**

Fig. 15 Effects of spacing on the side force generated by models AA and BB at $\delta_R = 30°$.

Thus far, the jet momentum coefficient, C_μ, was considered as the leading parameter affecting the state of the flow over the rudder because it is traditionally used when blowing is applied to control flow separation and increase the lift on wings. The length scales or area ratios used in the definition of C_μ may be unique for flapless 2D airfoils, but their uniqueness is lost when flaps and slats are introduced to airfoils and even more so for finite wings. In the case of a highly deflected rudder, it may be the rudder area that determines the momentum required to control the flow and not the area of the entire vertical tail. The use of fluidic oscillators emanating from discrete sources provides additional length scales of significance, for example, the size of the actuator's nozzles, their aspect ratio, and the distance between adjacent actuators, in addition to the actuator's characteristics that establish the jet's sweep angles and frequency. These parameters should be carefully considered when contemplating applications to commercial airplanes.

3. *Actuator Spacing*

The variations of C_{Yn} with C_μ are shown in Fig. 15 for $\delta_R = 30°$ and $3\% < Sp < 15\%$ on models AA and BB. For the smallest values of C_μ measurable (i.e., $C_\mu \approx 0.1\%$), an increase in C_{Yn} of 20% was recorded on model AA when the spacing $Sp < 9\%$. Every fifth actuator was used to generate the data obtained at $Sp = 15\%$ so that there was no possibility that adjacent fluidic oscillators would cover the entire rudder area and attach the flow to the surface. The same effect was observed on model BB but the values of ΔC_{Yn} realized were substantially smaller.

Increasing the distance between adjacent actuators at the subscale models revealed two interesting characteristics. At low levels of C_μ, the flow was sensitive to sparsely distributed actuators. A collective $C_\mu \approx 0.1\%$ was capable of increasing the side force generated by the rudder by 15% (Fig. 15). This result is achieved by reducing the spanwise flow induced by the large sweep back angle of the test article. Increasing the number of actuators and thus reducing the distance between adjacent actuators reduced the initial slope of $(\partial C_{Yn}/\partial C_\mu)$. When the actuator spacing was reduced to 3% of the span (32 actuators), the initial $(\partial C_{Yn}/\partial C_\mu) \approx 0$ at $\delta_R = 30°$. This may be attributed in part to the decrease in the velocity ratio between the jets and the free stream that is associated with an increase in the number of actuators used and a reduction in actuator-induced flow instability. This result provides the proof that C_μ, alone, does not govern the characteristics of the flow.

The side force for models AA and BB in Fig. 15 keeps increasing beyond $C_\mu > 0.8\%$ for all actuator spacings considered. For $C_\mu \leq 0.8\%$ actuators inhibit spanwise flow. The fluidic oscillator jets primarily prevent separation by providing strong streamwise vortices and larger surface coverage over the potential region of separated flow. A decrease in actuator spacing produces an increase in the AFC coverage area on the rudder. Therefore, 32 actuators ($Sp = 3\%$) provide the largest increase in ΔC_{Yn} at high C_μ.

Tuft pictures taken for the baseline case at $\beta = 0°$ and $\delta_R = 30°$ indicate that the flow over the rudder surface proceeds almost entirely along the span. This implies that the velocity component perpendicular to the leading edge near the surface is negligible and that the chordwise flow is either stagnated or separated (Fig. 16). It suggests that the boundary-layer flow turns in the spanwise direction to avoid the chordwise adverse pressure gradient and its associated deceleration. The change in the flow direction results in a low pressure of the deflected rudder (Fig. 5) and a large increase in the form drag that is very substantial at larger δ_R (Fig. 2). This explains why horizontal stabilizers that are required to provide negative lift in cruise use incidence for trim rather than deflected elevators that were used for trim in the 1940s and 1950s.

For the AA model, initial signs of reduced effectiveness occur at $\delta_R = 25°$ (Fig. 10a). These signs become more pronounced at $\delta_R > 30°$, which most likely determines the maximum effective rudder deflection. The tufts corresponding to the baseline flow condition (Fig. 16) are almost all directed along the span, particularly on the outboard half of the rudder. The tufts located near the rudder leading edge on its inboard portion still indicate an appreciable chordwise component of the flow. When the actuators are tightly spaced ($Sp = 3\%$), the direction of the flow near the surface changes gradually with increasing C_μ and almost uniformly along the span. Such a change in flow direction requires surpassing a threshold value of C_μ before being noticeable. This observation concurs with results shown in Fig. 15, where $\partial C_{Yn}/\partial C_\mu$ increases with increasing C_μ. The slope of $\partial C_{Yn}/\partial C_\mu$ is increasing for $Sp = 3\%$ and $C_\mu < 0.75\%$, which indicates that the nozzle jet velocity is starting with a lower value but is increasing quicker. For the same C_μ, the corresponding actuator plenum pressure is lower for the larger total nozzle area of the closely spaced actuators ($Sp = 3\%$), which means that the flow through the nozzle would eventually choke at a higher C_μ value. The opposite is true for the sparsely spaced actuators. At $C_\mu = 1.5\%$, most of the tufts point in the direction of the free stream (Fig. 16).

When every fifth actuator was active ($Sp = 15\%$) at $\delta_R = 30°$, an increase in C_{Yn} of approximately 20% was achieved at the smallest values of measurable C_μ (i.e., $C_\mu \approx 0.1\%$ as seen in Fig. 15). At this spacing, it was unlikely that adjacent fluidic oscillators would interact and cover a substantial fraction of the rudder area forcing two-dimensional type of reattachment of the flow to the surface. Thus, the main effect of the actuation is the redirection of the flow toward the direction of the free stream.

The jet velocities emanating from each nozzle of the six-actuator array are quite high even for relatively modest C_μ inputs due to the small number of the actuators used. Thus, the actuators create jet curtains that reduce or even eliminate locally the spanwise flow at higher values of C_μ. This is visible in Fig. 17, where the high-speed jets, marked by blue arrows downstream of the trailing edge of the rudder, penetrate the spanwise flow and deflect it along the entire rudder chord in the direction of the free stream. The flow just above each of the jets marked by the arrow is parallel to the freestream; however, in the vicinity of the trailing edge the flow starts to turn toward the tip. It proceeds to turn toward the span becoming parallel to the TE near the mid-distance between the actuators. Upstream of the trailing edge, the flow turns back toward the rudder hinge partly

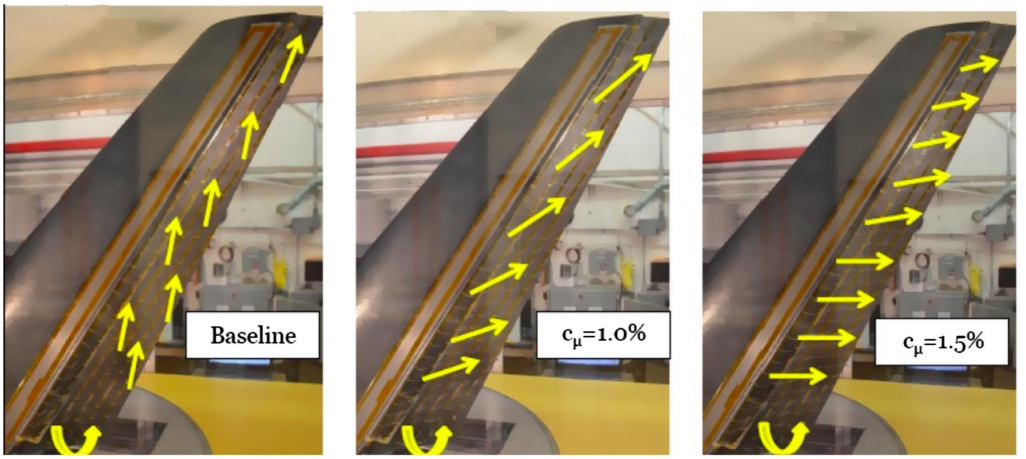

Fig. 16 Flow visualization on model AA rudder for $\beta = 0°$, $\delta_R = 30°$, $Sp = 3\%$ at increasing values of C_μ.

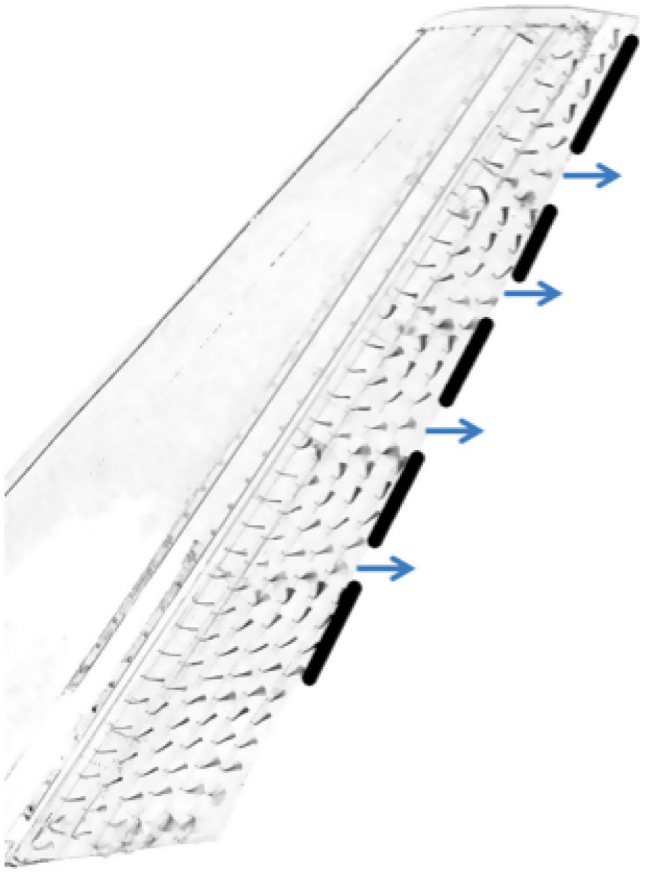

Fig. 17 Tuft visualization of surface flow over a deflected rudder with sparse actuation.

because of the low pressure in the hinge region and partly because of the strong entrainment by the jet emanating from the nozzle located outboard of the one considered. Therefore, cell-like flow is created between each pair of actuator jets that reduces the effectiveness of a large C_μ input at large Sp (see Fig. 15). This may be avoided by switching to closely spaced actuation whenever the need arises. This change may entail an increase in mass flow consumed that varies proportionally as the square root of the increased spacing, provided that the dimensions of the actuators do not change. One may consider changing the distribution of momentum along the span by increasing actuator size toward the tip, changing the pressure input to each individual actuator, and possibly even altering the location of successive actuators. The assessment of the additional parameters mentioned above needs to be performed when intending to integrate AFC into preliminary design.

C. Comparison Between Subscale and Full-Scale Models

The main objective of the full-scale wind tunnel test was to demonstrate the implementation of a sweeping jet AFC system on the vertical tail of a modern commercial transport. The AFC goal was to increase side force at maximum rudder deflection of 30° for 0° and −7.5° sideslip angles potentially occurring during takeoff. A successful demonstration of AFC technology is a major risk reduction step toward a flight demonstration. This test provided, for the first time, the opportunity to assess design and scaling issues for full-scale application of AFC and validation of subscale and CFD observations regarding the sensitivities and effects of AFC on the vertical tail of a commercial aircraft.

The full-scale model was a Boeing 757 vertical tail refurbished for testing at the $40' \times 80'$ National Full-Scale Aerodynamic Complex (NFAC) wind tunnel [28]. The model has 11 cutouts on both sides of the rudder leading edge (LE) to make room for the rudder support mechanism that allows rudder deflections in both yaw directions (Fig. 18a). The results presented in this section are focused on the configuration where the LE cutouts were covered in order to provide a better correlation with the Caltech subscale results. This configuration resembles the subscale model with a "clean rudder LE" (see Fig. 18b). The subscale tests provided AFC design and performance parameters guidance such as the actuator spacing. The scaling factor for the actuator size and spacing between subscale and full-scale models is 6.25, which roughly matches that of the model scaling. The AFC system of the full-scale model consisted of 37 fluidic oscillators evenly spaced across the starboard span. Each actuator had a nozzle width-to-height ratio of 2, and the spacing between each actuator was 16.7 times the nozzle width ($Sp = 2.85\%$). Each actuator oscillated at a frequency of approximately 250 Hz. The full-scale test confirmed the effectiveness of AFC and validated the scaling key parameter used, which was the C_μ.

Figure 19a shows a comparison of different baseline cases. The NFAC 434 and 476 cases represent a configuration with LE cutouts open. In this configuration, the rudder LE was plugged internally to minimize air leakage coming from underneath the model base support (blister) and through the rudder. NFAC 411 is a baseline configuration with cutouts covered to stop the undesirable air outflow (leakage) from inside the rudder and out through the cutouts completely. With the cutouts opened (NFAC 434 and 476), the rudder effectiveness decreased with increasing rudder deflection angle above 22.5°. The open area of each cutout increases with rudder deflection, as does the potential leakage (mass flow) through the cutouts and the associated detrimental effect on the side force that is most visible at $\delta_R > 22.5°$ (Fig. 19a, NFAC 434 and 476). These two runs represent the baseline for the uncovered LE cutouts. The addition of vortex generators near the rudder hinge (NFAC 498) produced the same enhancement of the side force as covering the

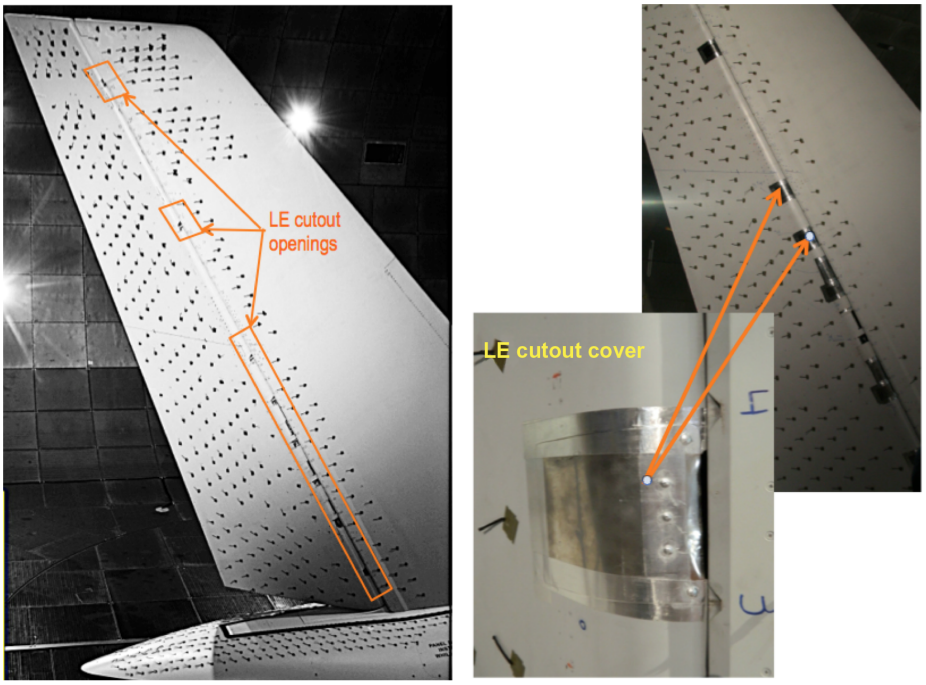

a) Rudder LE cutout openings b) Rudder LE with cutout covers installed

Fig. 18 Rudder leading edge cutouts and temporary covers.

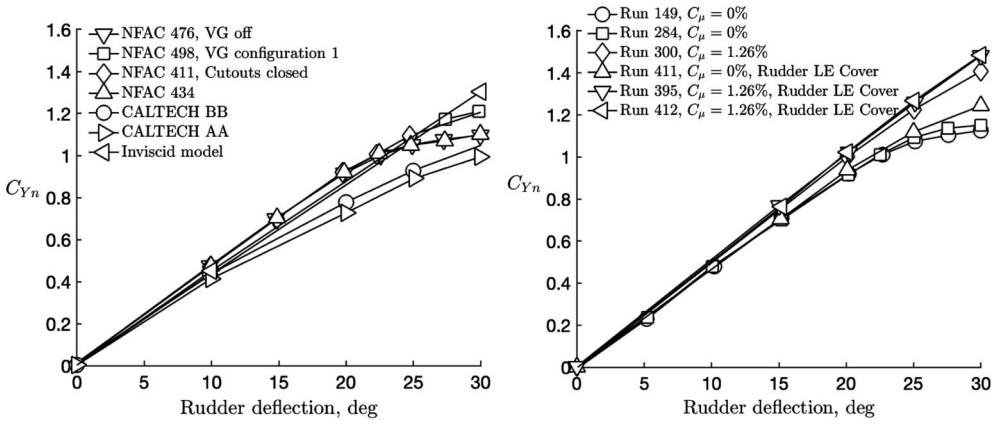

a) Baseline side force generated b) Full-scale model baseline and actuated side force generated

Fig. 19 Side force generated by the rudder for the full-scale and subscale model configurations at sideslip angle, $\beta = 0°$.

cutouts (NFAC 411). At $\delta_R > 22.5°$, the slope of the side-force curve $\partial C_{Yn}/\partial\delta_R$ was increased, providing an improvement of approximately 8% in C_{Yn} at $\delta_R = 30°$. It suggests that the vortex generators overcame some flow separation generated by the cutouts being open. The Caltech model AA generates substantially lower side force at all rudder deflections. This may be attributed to the Re effect that is an order of magnitude smaller on this model, but it does not explain why $\partial C_{Yn}/\partial\delta_R$ is larger on the subscale model for $\delta_R > 25°$ compared with the full-scale model. The difference in C_{Yn} generated by the two models (i.e., full-scale with LE cutouts opened and subscale with clean LE) was $\Delta C_{Yn} < 0.05$ at $\delta_R = 30°$ while being twice as large at $\delta_R = 20°$. The momentum lost in a turbulent boundary layer on a nonlifting flat plate decreases as $Re^{-0.2}$ at Re of the order of 10^6. One would expect that the flow will separate at a lower angle of attack on the Caltech models because the momentum loss due to friction increases with decreasing Re, but according to Fig. 19a, the opposite happens for baseline cases with cutouts opened/unsealed (NFAC 434 and 476) where flow separation is much more pronounced on the full-scale vertical tail at $\delta_R > 22.5°$. Thus, the major cause of the baseline difference may be the low-speed flow through the cutouts displacing the local boundary layer over the rudder that resulted in enhanced flow separation. Notice that blowing is useful when a high-speed jet entrains ambient fluid [6] and detrimental when a low-speed jet displaces it. Another possibility is the reduction of the rudder LE regions that could accelerate flow locally to produce suction pressures for side force enhancement.

The side force generated at different rudder deflections while using 18 evenly spaced actuators with and without the cutout covers at NFAC is plotted in Fig. 19b. The mass flow through the actuators was set to produce an aggregate C_μ of 1.26% at 100 knots (50 m/s). The test article was equipped with 37 actuators that were individually controlled, therefore many combinations were in principle possible. The total number of actuators and the selection of their size were predetermined by the pneumatic power available (pressure and mass flow) for the planned flight test aircraft. The initial CFD results indicated that a much larger amount of air was needed to approach the "inviscid limit," and so it was thus decided to maintain a large safety margin during the design stage of the full-scale test. Consequently, using half of the actuators installed is a representative case. AFC increased the rudder effectiveness at $\delta_R > 15°$ by maintaining $\partial C_{Yn}/\partial\delta_R$ almost constant up to the maximum possible rudder deflection of $\delta_R = 30°$. Thus, the maximum improvement in C_{Yn}

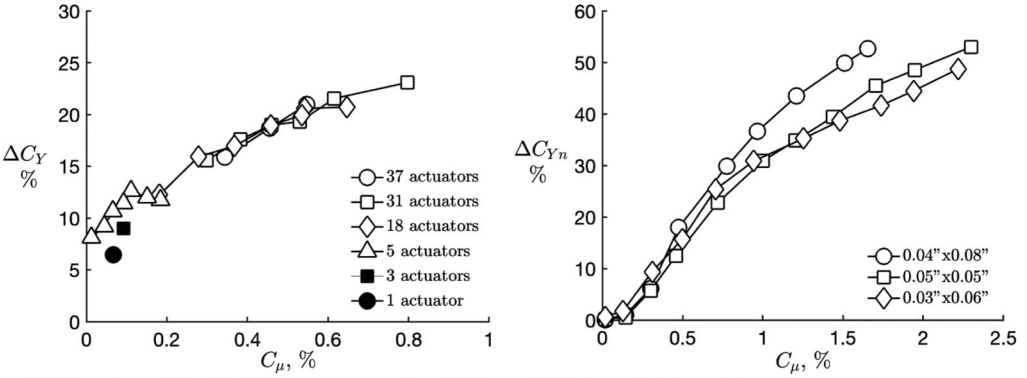

a) Full-scale model with LE cutout covered/sealed for different spacings **b) Sub-scale AA model**

Fig. 20 Dependence of side force on C_μ at $\delta_R = 30°$ and $\beta = 0°$.

measured for this level of input is $\Delta C_{Yn} = 0.22$ when the cutouts were sealed and $\Delta C_{Yn} = 0.32$ when they were open. It implies that the presence of the cutouts had a favorable effect on the side force generated by AFC because it deteriorated the baseline. This represents an improvement over the baseline values of 18% ($\Delta C_{Yn}/C_{Yn_{\text{Baseline}}}$) for the sealed cut outs and 29% for the open cutouts. It was stated in the previous section that $\Delta C_{Yn}/C_{Yn_{\text{Baseline}}}$ is an inappropriate criterion for measuring the success of AFC application to wings and this change in baseline data just confirms that statement. The ΔC_{Yn} measured on the BB model at Caltech when a similar number of actuators were used was also 0.21, corresponding to $C_\mu = 1.26\%$ (Fig. 15); thus the additional control authority provided by AFC seems to be *Re* independent. This hypothesis needs to be further verified, but it could be expected due to the inviscid instability mechanism that governs the flow between adjacent sweeping jets.

In Fig. 20a at 30° rudder deflection and at low levels of C_μ, the slope $\partial \Delta C_{Yn}/\partial C_\mu$ is only slightly dependent on the number of actuators used, provided that the latter is equal or larger than 18. When the number of actuators was decreased to 5, $\partial \Delta C_{Yn}/\partial C_\mu$ decreased for $C_\mu > 0.1\%$ rather than increased as was observed with subscale models. An inflection point as seen in Fig. 15 was never observed in the results for the full-scale model. Clearly there is no crossover point among the various curves at a prescribed value of C_μ. Additional observations between the subscale models (Fig. 15) and full-scale results (Fig. 20a) are detected at high C_μ values. For the subscale models, an increase in C_μ results in a concomitant increase in C_{Yn}, particularly for closely spaced actuators. A similar increase is observed on the full-scale model. The increase in number of actuators used reduces the efficiency of AFC but enables the attainment of higher levels of ΔC_{Yn} at $\delta_R = 30°$. The data present similarities using closely spaced actuators on both models, that is, full-scale and subscale (Fig. 20), for a $C_{Yn} = 20\%$ at C_μ values from 0.55% to 0.65%, respectively. The full-scale configurations having 18 actuators or more reached our 20% side force increase target using actuators with a nozzle width-to-height ratio of 2, which was the same ratio of two of the actuators used in the subscale test. This suggests that C_μ is a useful parameter for scaling fluidic oscillators from subscale to full-scale tests.

IV. Conclusions

In recent years, fluidic oscillators have been employed as an active flow control (AFC) actuator of choice in laboratory-scale applications, and this paper highlights the recent research efforts to use this technology for side force augmentation on the vertical tail of a commercial transport aircraft. AFC subscale experiments were conducted using four generic vertical tail models of slightly different planforms, where fluidic oscillators were applied to a vertical stabilizer (swept back wing) with a rudder (simple flap). The actuators were installed at the rudder hinge along the trailing edge of the main element (stabilizer) due to convenience of application on an airplane. Fluidic oscillators have been shown to behave somewhat akin to vortex generators, but they also add momentum to the flow and manage to redirect it, thus improving the overall rudder performance well beyond that of a simple, passive system. Perhaps most striking in this application is the effect on side force and its associated drag before flow separation, suggesting that simply redirecting flow in the streamwise direction is an effective side force generation tool.

The differences in overall performance as a function of spacing were significant among the parameters studied. The large spacing of $Sp = 15\%$ produced approximately a 20% side force increase with an input of $C_\mu \approx 0.1\%$. Flow visualization suggested that large spacing redirects the flow instead of reducing or controlling separation. This shows promise, but one needs to consider the available power (e.g., to provide supply air pressure and mass flow rate) on a commercial transport aircraft. Smaller spacing showed a different behavior, where a low $C_\mu = 0.1\%$ input provided no side force enhancement, but an order of magnitude larger C_μ input increased the side force in excess of 50%. Large-spacing actuation is more efficient at small C_Π, and small-spacing actuation is more effective at large C_Π.

Another parameter evaluated in this study was the model planform geometry. A common practice for most experiments associated with AFC has followed the objective to improve the performance of a prescribed specific geometry. The underlying philosophy of the prevailing approach is defined by the success criteria as supported by our recent full-scale tests [29,30], which seek certain percentage improvement on a given configuration. There is a close coupling among the variables affecting C_{Yn}. There are the traditional ones such as those applied to airfoils (camber, thickness, and incidence) and to wings (wing-planform, aspect ratio, sweep, taper, and twist), and there are new ones associated with AFC. The jury is still out for the best AFC system to be used (i.e., the selection of actuation) and there is a wide variety of options and categories available. But even if one selects the type of actuation, there is still a broad range of parameters to be used and optimized due to significant interaction between surface design and actuation. AFC should be considered in the preliminary design process as it could enable wings having larger camber without separation or larger control surface deflection.

Leveraged on knowledge gained from the subscale tests, a full-scale test was carried out subsequently. A threshold success criterion of 20% increase in the maximum side force was exceeded at largest rudder deflection (30°) using 18 or more sweeping jet actuators in the absence of sideslip at a momentum coefficient input of approximately 0.55%. Both subscale and full-scale tests showed a 20% side force increase corresponding to similar C_μ (≈0.65% and ≈0.55%, respectively) for the fluidic oscillators of the similar design and spacing, which confirms that C_μ is a reasonably good parameter to use for scaling-up of AFC actuators from subscale to full-scale tests. The successful full-scale wind tunnel testing of this AFC application (i.e., achieving the side force increase of 20% or greater) cleared the way for a subsequent flight demonstration on the Boeing 757 ecoDemonstrator in 2015 [31].

Most of the results presented used momentum coefficient, C_μ, as the primary input. However, this is not a unique parameter driving the design of an AFC system [32–34] but certainly needs to be considered

during the initial stages of design. It determines the amount of mass flow required for selecting size, layout, and number of actuators. This parameter was also found to be a useful for scaling-up fluidic oscillator AFC systems from subscale to full-scale wind tunnel tests. Nevertheless, C_μ does not contain the supply air pressure information, which is also important in determining the pneumatic power usage of an AFC system. The power coefficient, C_Π, which contains both the mass flow and pressure information, is an equitable parameter to use for comparing the power consumption of AFC systems. In addition, one should also include other parameters in the evaluation of AFC designs, such as the actuator size, weight, and complexity.

References

[1] Attinello, J. S., "Design and Engineering Features of Flap Blowing Installations," edited by G. V. Lachmann, *Boundary Layer, and Flow Control: Its Principles, and Application*, Vol. 1, Pergamon Press, New York, 1961, pp. 463–515.

[2] Stratford, B. S., "Early Thoughts on the Jet Flap," *Aeronautical Quarterly*, Vol. 7, No. 1, Feb. 1956, pp. 45–59. doi:10.1017/S000192590001012X

[3] Poisson-Quinton, P., and Lepage, L., "Survey of French Research on the Control of Boundary Layer and Circulation," *Boundary Layer, and Flow Control: Its Principles, and Application*, edited by G. V. Lachmann, Vol. 1, Pergamon Press, New York, 1961, pp. 21–73.

[4] Chen, C., Seele, R., and Wygnanski, I., "Separation and Circulation Control on an Elliptical Airfoil by Steady Blowing," *AIAA Journal*, Vol. 50, No. 10, 2012, pp. 2235–2247. doi:10.2514/1.J051538

[5] Chen, C., Seele, R., and Wygnanski, I., "Flow Control on a Thick Airfoil Using Suction Compared to Blowing," *AIAA Journal*, Vol. 51, No. 6, 2013, pp. 1462–1472. doi:10.2514/1.J052098

[6] Wygnanski, I., and Newman, B. G., "The Effect of Jet Entrainment on Lift and Moment for a Thin Aerofoil with Blowing," *Aeronautical Quarterly*, Vol. 15, No. 2, 1964, pp. 122–150. doi:10.1017/S0001925900003085

[7] Wygnanski, I., "A Wind Tunnel Investigation of a Thin Aerofoil with a Sharp Leading Edge, and Blowing Applied at the Midchord at Two Angles Relative to the Surface," *The Journal of the Royal Aeronautical Society*, Vol. 70, No. 666, 1966, pp. 665–669. doi:10.1017/S0001924000057511

[8] Woszidlo, R., Nawroth, H., Raghu, S., and Wygnanski, I., "Parametric Study of Sweeping Jet Actuators for Separation Control," AIAA Paper 2010-4247, June 2010. doi:10.2514/6.2010-4247

[9] Woszidlo, R., and Wygnanski, I., "Parameters Governing Separation Control with Sweeping Jet Actuators," AIAA Paper 2011-3172, June 2011. doi:10.2514/6.2011-3172

[10] Childs, R. E., Stremel, P. M., Garcia, J. A., Heineck, J. T., Kushner, L. K., and Storms, B. L., "Simulation of Sweep-Jet Flow Control, Single Jet and Full Vertical Tail," AIAA Paper 2016-0569, 2016. doi:10.2514/6.2016-0569

[11] Oster, D., and Wygnanski, I., "The Forced Mixing Layer Between Parallel Streams," *Journal of Fluid Mechanics*, Vol. 123, Oct. 1982, pp. 91–130. doi:10.1017/S0022112082002973

[12] Monkewitz, P. A., and Huerre, P., "Influence of the Velocity Ratio on the Spatial Instability of Mixing Layers," *Physics of Fluids*, Vol. 25, No. 7, July 1982, pp. 1137–1143. doi:10.1063/1.863880

[13] Neuburger, D., and Wygnanski, I., "The Use of a Vibrating Ribbon to Delay Separation on Two-Dimensional Airfoils: Some Preliminary Observations," *Proceedings in Workshop II on Unsteady Separated Flow*, edited by J. M. Walker, U.S. Air Force Systems Command, Frank J. Seiler Research Lab. Rept. FJSRL-TR-88-0004, 1988, pp. 333–341.

[14] Seifert, A., Bachar, T., Koss, D., Wygnanski, I., and Shepshelovich, M., "Oscillatory Blowing: A Tool to Delay Boundary-Layer Separation," *AIAA Journal*, Vol. 31, No. 11, 1993, pp. 2052–2060. doi:10.2514/3.49121

[15] Glezer, A., and Amitay, M., "Synthetic Jets," *Annual Review of Fluid Mechanics*, Vol. 34, No. 1, 2002, pp. 503–529. doi:10.1146/annurev.fluid.34.090501.094913

[16] Sahni, O., Wood, J., Jansen, K. E., and Amitay, M., "3-D Interactions Between a Finite-Span Synthetic Jet and a Cross Flow at a Low Reynolds Number and Angle of Attack," *Journal of Fluid Mechanics*, Vol. 671, March 2011, pp. 254–287. doi:10.1017/S0022112010005604

[17] Rathay, N. W., Boucher, M. J., Amitay, M., and Whalen, E., "Performance Enhancement of a Vertical Tail Using Synthetic Jet Actuators," *AIAA Journal*, Vol. 52, No. 4, 2014, pp. 810–820. doi:10.2514/1.J052645

[18] Post, M. L., and Corke, T. C., "Separation Control on High Angle of Attack Airfoil Using Plasma Actuators," *AIAA Journal*, Vol. 42, No. 11, 2004, pp. 2177–2184. doi:10.2514/1.2929

[19] Greenblatt, D., and Wygnanski, I., "The Control of Flow Separation by Periodic Excitation," *Progress in Aerospace Sciences*, Vol. 36, No. 7, 2000, pp. 487–545. doi:10.1016/S0376-0421(00)00008-7

[20] Seifert, A., Bachar, T., Wygnanski, I., Kariv, A., Cohen, H., and Yoeli, R., "Application of Active Separation Control to a Small Unmanned Air Vehicle," *Journal of Aircraft*, Vol. 36, No. 2, 1999, pp. 474–477. doi:10.2514/2.2457

[21] McVeigh, M. A., Nagib, H., Wood, T., and Wygnanski, I., "Full-Scale Flight Tests of Active Flow Control to Reduce Tiltrotor Aircraft Download," *Journal of Aircraft*, Vol. 48, No. 3, 2011, pp. 786–796. doi:10.2514/1.46956

[22] Vatsa, V., Koklu, M., and Wygnanski, I., "Numerical Simulation of Fluidic Actuators for Flow Control Applications," AIAA Paper 2012-3239, June 2012. doi:10.2514/6.2012-3239

[23] Hirsch, D. G., Graff, E. C., and Gharib, M., *Compressible Flows in Fluidic Oscillators*, 2013, arXiv preprint arXiv:1310.3310.

[24] Mooney, H. P., Brandt, J. B., Lacy, D. S., and Whalen, E. A., "AFC-Enabled Vertical Tail System Integration Study," NASA CD-2014-218168, March 2014.

[25] Seele, R., Graff, E., Gharib, M., Taubert, L., Lin, J., and Wygnanski, I., "Improving Rudder Effectiveness with Sweeping Jet Actuators," AIAA Paper 2012-3244, June 2012. doi:10.2514/6.2012-3244

[26] Isaacs, D., "Wind Tunnel Measurements of the Low Speed Stalling Characteristics of a Model of the Hawker-Siddeley Trident 1C," RAE, Bedford, Tech. Rept. 68108, (ARC 30775), Bedford, 1968.

[27] Anderson, J. D., "Incompressible Flow over Airfoils," *Fundamentals of Aerodynamics*, 3rd ed., McGraw–Hill, New York, 2001.

[28] NASA Ames Research Center Aeromechanics, "40- by 80-/80- by 120-Foot Wind Tunnels," http://www.nasa.gov/centers/ames/research/lifeonearth/lifeonearth-windtunnels.html.

[29] Whalen, E. A., Lacy, D., Lin, J. C., Andino, M. Y., Washburn, A. E., Graff, E. C., and Wygnanski, I. J., "Performance Enhancement of a Full-Scale Vertical Tail Model Equipped with Active Flow Control," AIAA Paper 2015-0784, Jan. 2015. doi:10.2514/6.2015-0784

[30] Andino, M. Y., Lin, J. C., Washburn, A. E., Whalen, E. A., Graff, E. C., and Wygnanski, I. J., "Flow Separation Control of a Full-Scale Vertical Tail Model Using Sweeping Jet Actuators," AIAA Paper 2015-0785, Jan. 2015. doi:10.2514/6.2015-0785

[31] Whalen, E. A., Shmilovich, A., Spoor, M., Tran, J., Vijgen, P., Lin, J. C., and Andino, M. Y., "Flight Test of an Active Flow Control Enhanced Vertical Tail," *AIAA Journal*, Vol. 56, No. 9, 2018, pp. 3393–3398. doi:10.2514/1.J056959

[32] Woszidlo, R., "Parameters Governing Separation Control with Sweeping Jet Actuators," Dissertation, The Univ. of Arizona, Tucson, AZ, 2011, http://hdl.handle.net/10150/203475.

[33] Nagib, H., Kiedaisch, J., Reinard, P., and Demanett, B., "Control Techniques for Flows with Large Separated Regions: A New Look at Scaling Parameters," AIAA Paper 2006-2857, June 2006. doi:10.2514/6.2006-2857

[34] Stalnov, O., and Seifert, A., "On Amplitude Scaling of Active Separation Control," *Active Flow Control II. Notes on Numerical Fluid Mechanics and Multidisciplinary Design*, edited by R. King, Vol. 108, Springer, Berlin, 2010, pp. 63–80. doi:10.1007/978-3-642-11735-0_5

D. Greenblatt
Associate Editor